ACS APPLIED MATERIALS & INTERFACES

www.acsami.org

Research Article

Flexible Materials for High-Resolution 3D Printing of Microfluidic Devices with Integrated Droplet Size Regulation

Niclas Weigel, Max J. Männel, and Julian Thiele*

Cite This: *ACS Appl. Mater. Interfaces* 2021, 13, 31086–31101

Read Online

ACCESS | Metrics & More | Article Recommendations | Supporting Information

ABSTRACT: We develop resins for high-resolution additive manufacturing of flexible micromaterials via projection microstereolithography (PμSL) screening formulations made from monomer 2-phenoxyethyl acrylate, the cross-linkers Ebecryl 8413, tri(propyleneglycol) diacrylate or 1,3,5-triallyl-1,3,5-triazine-2,4,6-(1*H*,3*H*,5*H*)-trione, the photoabsorber Sudan 1, and the photoinitiator diphenyl(2,4,6-trimethylbenzoyl)phosphine oxide. PμSL-printed polymer micromaterials made from this resin library are characterized regarding achievable layer thickness depending on UV exposure energy, and for mechanical as well as optical properties. The best-candidate resin from this screening approach allows for 3D-printing transparent microchannels with a minimum cross section of approximately 35 × 46 μm^2, which exhibit proper solvent resistance against water, isopropanol, ethanol, *n*-hexane, and HFE-7500. The mechanical properties are predestined for 3D-printing microfluidic devices with integrated functional units that require high material flexibility. Exemplarily, we design flexible microchannels for on-demand regulation of microdroplet sizes in microemulsion formation. Our two outlines of integrated droplet regulators operate by injecting defined volumes of air, which deform the droplet-forming microchannel cross-junction, and change the droplet size therein. With this study, we expand the library of functional resins for PμSL printing toward flexible materials with micrometer resolution and provide the basis for further exploration of these materials, e.g., as microstructured cell-culturing substrates with defined mechanics.

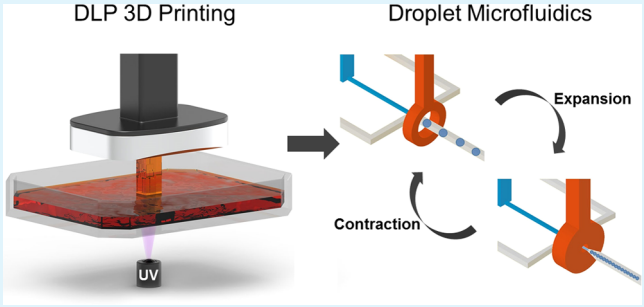

KEYWORDS: *3D printing, stereolithography, photopolymerization, microfluidics, emulsions*

1. INTRODUCTION

Microfluidic devices are commonly fabricated by a combination of photo- and soft lithography.[1] Starting from a structure-bearing photomask, the desired microchannel network is transferred via UV-light exposure of a photoresist onto a silicon or glass substrate. After baking and the development of the microchannels, polydimethylsiloxane (PDMS) is employed to produce a replica of the microchannels that is sealed by another PDMS layer or a glass slide, commonly utilizing plasma activation. This procedure can take up to several days depending on the experimental skills of the user and the available infrastructure, before a functional microfluidic device is obtained. Despite the multitude of applications of microfluidics in sensing,[2−4] cell culturing,[5−8] sorting and mixing,[9,10] high-throughput drug screening,[11−14] or the preparation of emulsions and vesicles,[15] this multistep fabrication process is one major reason that has long limited the commercial breakthrough of microfluidics. On this account, additive manufacturing techniques have started to revolutionize the fabrication of microfluidic devices due to the freedom of digital design and, under ideal conditions, the one-step processability of starting materials such as polymer melts, hydrogel precursors, or photopolymer formulations (resins).[16−18] Especially, digital light processing (DLP)-based 3D printing or projection microstereolithography (PμSL) exhibits a number of promising features that may soon replace well-established techniques for microfluidic device fabrication. PμSL combines short fabrication times ranging from just minutes to hours,[19,20] a large variety of processable materials offering special properties and functions,[21−27] the ability to combine multiple materials in one fabrication process,[28−30] as well as access to highly resolved and complex 3D geometries.[31,32] Control over key material properties of microfluidic devices, such as micron-scale structural resolution and surface roughness, is exerted via PμSL by the material composition of photocurable resins, illumination parameters, as well as printing direction and separation distance, as shown in recent studies, including ones by our group.[33−37]

Received: March 25, 2021
Accepted: June 8, 2021
Published: June 26, 2021

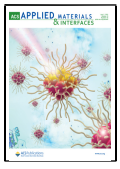

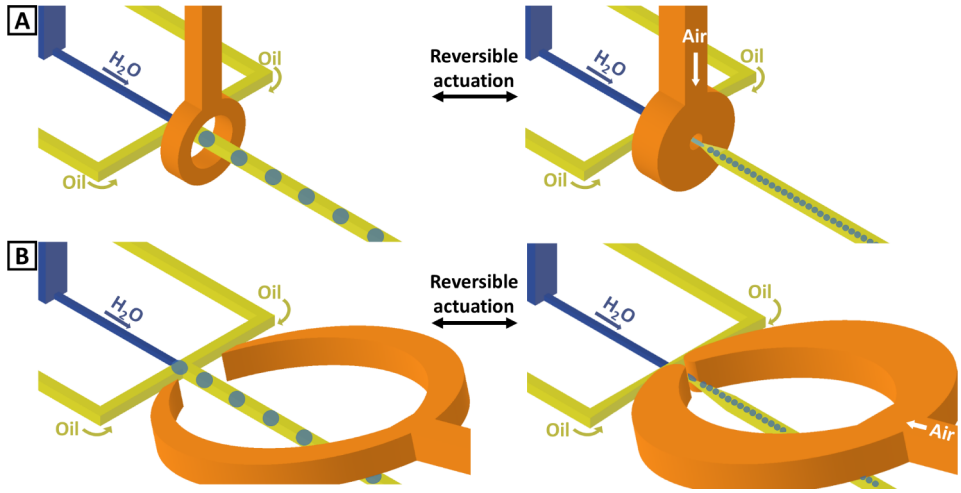

Figure 1. Concept of integrated droplet regulators in PμSL-printed flexible microfluidic devices with (A) a ring shape and (B) a pliers shape. During formation of water-in-oil (W/O) emulsions stabilized by a surfactant, either regulator is activated via injection of a defined air volume into the regulator unit. Upon expansion, the droplet-transporting microchannel directly behind the droplet-forming microchannel junction area as well as the continuous-phase channel dimensions are compressed either from all sides (ring-shaped regulator) or from two facing sides (pliers-shaped regulator) allowing for manipulating the microdroplet diameter.

While initially, PμSL fabrication for microfluidics primarily focused on flow cell design for passive fluid flow control, the integration of functional valves and pumps, e.g., for actively controlling fluid flow by reversible microchannel blockage has been realized.[38−40] Nordin and coworkers utilized PμSL for fabricating polyethylene glycol diacrylate (PEGDA)-based microfluidic devices with integrated valves. Here, the authors used a pressurized chamber to deflect a few micrometer-thick membrane to repeatedly open and close nearby flow channels up to 800 cycles without major changes in performance.[41] Folch and coworkers followed a similar approach utilizing PμSL to 3D-print valves inspired by the work of Quake and coworkers.[42] Again, utilizing a "homemade" PEGDA-based resin for microfluidic device design, the authors proved their valves' durability by repeated actuation, and combined arrays of 64 valves within one microfluidic device to function as a microfluidic pump. Our group also investigated different "homemade" resins and their suitability for fabricating valves following Nordin's and Quake's design. Here, we were able to 3D-print a tri(propyleneglycol) diacrylate (TPGDA)-based resin with membrane thicknesses of 40 and 100 μm, respectively.[43] Although these 3D-printed thin membranes can be repeatedly deflected, a sufficiently large membrane diameter of 0.5 mm up to several millimeters is required for the membrane layer to deform. Additionally, the low ductility of these materials may limit the applicability for more complex valve designs and functions.

A prominent example of DLP-based 3D-printing of elastic, PDMS-like materials was presented by the Folch group in 2018, where 3D-printed methacryloxypropyl-terminated PDMS exhibited similar material properties as native PDMS such as high transmittance close to 100% and similar mechanical properties such as the common, commercial PDMS source Sylgard 184 (E = 520−937 kPa).[44] While these material properties are well-suited for microfluidic applications, the reported channel voids in microfluidic devices were 500 μm wide. In a recent example by Gonzalez et al., commercially available PDMS-acrylate was 3D-printed into microfluidic devices with minimum internal feature sizes of 400 μm.[45] Further examples for elastic, DLP-processed materials, which do not relate to microfluidics, were also made from urethane diacrylates. For instance, in 2017, Magdassi and coworkers processed commercial polyurethane acrylates (Ebecryl 8413) by PμSL into 3D-printed materials with Young's moduli ranging from 0.58 to 4.21 MPa and elongations at break of up to 1100%.[46] The fabrication process had to be carried out with a custom-made 3D printer at elevated temperatures of 70 °C, which is normally not feasible for commercial 3D printers. Another example is the work by Ge and coworkers, where the commercial resins TangoPlus and Ebecryl 113 were combined, corresponding 3D-printed parts mechanically analyzed depending on the amount of photoabsorber Sudan 1 (Sud1), and applied as miniaturized soft robotic prototypes.[47] Generally, the reported 3D-printed elastic materials often seem to lack high resolution for inner-laying channel structures and thus are barely suitable for replacing conventional PDMS-based microfluidics that demands high-resolved structures in the sub-100-μm range.

On this account, we develop a library of acrylic- and allyl-based resins for PμSL to fabricate flexible materials with low elastic moduli of E < 0.7 MPa and elongations at break from 82 ± 17% to 1167 ± 106% that are truly comparable to PDMS with the reported Young's moduli ranging from 0.7 to 2.4 MPa, and elongations ranging from 122% to 567%.[48] To obtain large deformations inside our 3D-printed flow cells to act as droplet regulators, we aim at softer and stretchable materials compared to native PDMS to obtain a material basis that is more suitable for an advanced membrane or valve system. The resin library is made from 2-phenoxyethyl acrylate (POEA) as the reactive monomer combined with one of three different cross-linkers, namely, Ebecryl 8413, an aliphatic urethane diacrylate, 1,3,5-triallyl-1,3,5-triazine-2,4,6(1*H*,3*H*,5*H*)-trione (TATATO), and TPGDA. Optimized resin formulations are then utilized for fabricating microfluidic devices with an integrated functional unit that strongly relies on tunable material elasticity, optical transparency, and micron-sized feature sizes, namely, the fabrication of microfluidic devices with air-pressure-actuated membranes. Single microfluidic drop makers with a static microchannel layout only allow for forming a rather limited range of individual emulsion droplet sizes, controlled by

https://doi.org/10.1021/acsami.1c05547
ACS Appl. Mater. Interfaces 2021, 13, 31086−31101

adjusting the flow ratios of the respective phases. This conventional approach may not be feasible for specialized microfluidics experiments such as on-chip mixing of two reactive species in hydrogel formation or when using non-Newtonian fluids. By utilizing 3D-printed, deflectable membranes that compress the droplet-forming junction area and allow for addressing individual emulsion droplet sizes, we find two advantages of the presented method. (1) Both the fabrication process of flow cells via additive manufacturing as well as the use of one single flow cell for multiple experiments saves a significant amount of time. (2) PμSL printing and the ability to change fluid flow conditions on demand reduces material consumption by requiring only one flow cell instead of several devices and due to faster fluid flow stabilization compared to starting up one flow cell for each experiment. The here presented flow cells with integrated, flexible membrane can be expanded by defined amounts of air injected in a controlled fashion leading to a contraction of the droplet-forming channel. Inspired by the work by Abate et al., where a valve was integrated inside a PDMS-based microfluidic device to control droplet sizes and their formation frequency upon applying controlled pressure,[49] we evaluate two different types of integrated membrane designs that both act as regulators of droplet size in microemulsion formation. 3D-printing such droplet regulators combines the ease of device fabrication by high-resolution additive manufacturing with simplified access to emulsion formation by functional microfluidics.

In our first microfluidic device design, a ring-shaped valve is PμSL-printed surrounding a microchannel cross-junction for emulsion formation via flow-focusing (Figure 1A). With this single microfluidic device, we tune the emulsion droplet diameter over a wide range from 443 ± 5 μm down to 58 ± 3 μm. To highlight the variability in microchannel design via PμSL, a second droplet regulator is designed comprising two single void strands, which are uniformly activated to compress the microchannel junction area. Again, monodisperse emulsion droplets ranging from 412 ± 3 μm down to 128 ± 4 μm can be formed by controlled inflow of air into this pliers-shaped regulator (Figure 1B). Both droplet regulator designs can be actuated multiple times yielding droplet sizes for a given air volume in a reproducible fashion, as shown by the droplet changes upon five cycles of air injection and withdrawal exemplarily.

2. EXPERIMENTAL SECTION

2.1. Materials for 3D Printing. All chemicals are used as received unless otherwise noted. We use POEA (TCI chemicals, >93%) as a monomer and TATATO (Sigma-Aldrich, 98%), TPGDA (mixture of isomer s, Sigma-Aldrich), and Ebecryl 8413 (E8413, Allnex) as cross-linkers. In addition, we use Sud1 (Sigma-Aldrich, ≥95%) as a photoabsorber and diphenyl(2,4,6-trimethylbenzoyl)phosphine oxide (TPO, Sigma-Aldrich, 97%) as a photoinitiator, which are common base materials for UV-based 3D-printing methods.[50−53] Red-colored dye Sud1 increases the light absorption of a resin at wavelengths from 300 to 550 nm,[35] and TPO shows an absorption maximum from 325 to 415 nm.[54] The resins are prepared by adding the components to POEA, followed by vortexing and ultrasonication for approximately 15 min until the solid content is completely dissolved. Isopropyl alcohol (IPA), ethanol (EtOH), and acetone are used for postprocessing the 3D-printed green parts.

2.2. Spot Test Measurements. An Asiga Pico 2 HD (Asiga, Alexandria, Australia) is used for screening the achievable minimal structural height of test prints for different exposure energies and for eventually fabricating microfluidic devices from optimized process parameters and resin compositions. The PμSL printer has a LED light source emitting at a wavelength of 385 nm with an intensity of 46.3 mW cm^{-2}. The theoretical lateral resolution of the printer is 27 μm (X and Y pixel resolutions), and the layer thickness in Z axis can be set from 1 to 410 μm. Image formation in plane is based on a DLP with a 1920 × 1080 micromirror array. For spot tests, as-prepared resins are poured onto a glass slide that is cleaned with IPA and a precision tissue, and a light spot of the printer's UV light source with a diameter of 1.415 mm then exposes a certain spot of the resin to polymerize the illuminated volume. This procedure is repeated for different exposure times and photopolymer formulations. Excess resin is removed by flushing with acetone and vigorous flushing with IPA. Afterward, the samples are dried in open air for several hours. To determine the height of cured polymer spots, we use confocal microscopy (μsurf, Nanofocus AG, Oberhausen, Germany). Confocal images of the cured spots were taken at a pitch of 0.469 μm (objective 10×, standard HDR algorithm, exposure of 40 ms). The z range is set from the top of the clean glass slide (minimum value) to the top of the cured spot (maximum value). Both limits are determined by visible light reflection of both materials in confocal mode. The height profile was then extracted utilizing the provided software (μsurf analysis 7, Nanofocus AG).

2.3. Tensile Tests. For mechanical measurements, dog bones (50 mm by 15 mm by 0.5 mm) are 3D-printed with a layer thickness of 50 μm and exposure times of 8−20 s in X and Y directions to ensure sufficient adhesion of the 3D-printed material to the building platform. The 3D-printed dog bones are postprocessed by rinsing with IPA and EtOH and postcuring by an Otoflash G171 (NK-Optik GmbH) at 1000 flashes. Tensile tests compliant with DIN EN ISO 527-2/S3/1 are carried out with a Zwick-Z010 (ZwickRoell GmbH & Co. KG, Ulm, Germany) with a 10 N load cell and a traverse displacement transducer, starting with 0.1 N initial load and 10 mm min^{-1} test velocity, followed by a measured strain velocity of 10 mm min^{-1}. Values for the elastic modulus, the elongation at break, as well as the maximum stresses are determined for dog bone samples prepared from the corresponding resin formulations such as E7.5 (five samples), E15 (five samples), TP2.5 (five samples), TP5 (four samples), TA20 (seven samples), and TA40 (five samples).

2.4. Transmittance Measurements. Cuboidal objects with dimensions of 30 × 20 × 0.5 mm^3 are 3D-printed in X, Y plane without the addition of supports. The printed parts are then postprocessed by washing with EtOH before placing them on glass slides that are pretreated with ultrasound in an IPA bath for 10 min and dried in an air stream. Afterward, the 3D-printed objects are placed on individual glass slides, followed by shortly heating them to 50 °C to evaporate EtOH and ensure that the samples adhere air bubble-free to the glass slide based on their intrinsic stickiness. The 3D-printed samples are then stored light-protected at room temperature for several hours to cool down to room temperature. Finally, two 3D-printed samples of each resin formulation are placed into a four-well plate (polystyrene, Cellstar) and inserted into a plate reader (Infinite 200 Pro, TECAN). Here, the absorption spectra are measured at five spots on each sample (25 flashes for each spot) with wavelength steps of 3 nm from 300 to 950 nm. Three spots are measured on the respective glass slide being the blank measurement. To determine the transmittance of the 3D-printed objects, the average absorption of the blank measurement (N = 3) is subtracted from the average absorption of the sample (N = 5) plus the glass slide giving the effective absorption A of the pure resin material. Transmittance for each sample is calculated with the formula: $T = 10^{-(A)} \times 100$. The average transmittances of each resin type and their corresponding standard deviations are depicted in the transmittance spectra (Figure 4A). Optical doses greater than 4 at wavenumbers from 390 to 520 nm are partially not detected due to the high absorption of Sud1 and TPO.

2.5. Rheology, Scanning Electron Microscopy, Swelling Tests, and FTIR Analysis. Viscosity measurements of resin formulations are conducted on an MCR 301 rheometer (Anton Paar) using a cone plate (r = 25 mm, cone angle = 1°) at 25 °C with shear rates from 1 to 1000 s^{-1}.

https://doi.org/10.1021/acsami.1c05547
ACS Appl. Mater. Interfaces 2021, 13, 31086−31101

Scanning electron microscopy (SEM) measurements are performed with a Neon 40 EsB (Zeiss, field emission gun) at 3 kV. Images are recorded utilizing different detectors (SE2, InLens) at tilting angles of 0° and 45°.

For swelling tests, 3D-printed samples with a diameter of 10 mm and a thickness of 1 mm are postprocessed as described above and immersed, either in H_2O (Milli-Q), IPA (Fisher-Scientific, ≥99.8%), EtOH (VWR chemicals, absolute), dimethyl sulfoxide (DMSO, Sigma-Aldrich, >99.9%), tetrahydrofurane (THF, Acros Organics, for analysis), toluene (Acros Organics, for analysis), *n*-hexane (Merck, for analysis), and hydrofluorether (HFE) (3M Novec 7500, >99%). After t = 1, 3, and 24 h, samples submerged in the respective solvent are placed on a glass slide followed by immediate measurement of the sample diameters in X and Y directions using a digital high-precision calliper with an accuracy of 0.01 mm. The average diameter is then used to calculate the respective swelling ratio by $sr = (d_t - d_0)/d_0 \times 100$ with d_t being the sample diameter after the respective immersion time and d_0 being the initial diameter of the 3D-printed sample at t = 0 h.

FTIR spectra are recorded in the range of 4000−600 cm^2 with the spectrometer Vertex 80v (Bruker) in ATR-mode (Golden Gate Diamond ATR unit, SPECAC) with a spectral resolution of 4 cm^{-1} and 100 scans per measurement. Here, FTIR spectra of POEA, TATATO, as-prepared TA20, as well as an UV-polymerized layer of TA20 (exposure time of 15 s, rinsed with IPA) are compared and the bands are interpreted and assigned via ref 55.

2.6. 3D Printing of Microfluidic Devices. 3D test objects and microfluidic devices are designed with Autodesk Inventor. All 3D-printed microfluidic devices are fabricated with the microchannel transporting the dispersed phase during emulsion formation being perpendicular to the X, Y plane. The test devices for transmittance experiments are designed with the microchannels for the continuous phase being 400 × 400 μm^2 and for the dispersed phase being 200 × 200 μm^2. These 3D-printed devices are fabricated with an exposure time of 5 s at a set layer thickness of 25 μm. To determine the minimum internal feature size feasible for each resin formulation, test objects are 3D-printed with an exposure time of 4 s at a set layer thickness of 25 μm, with designed channel cross-sections of 54 × 54, 81 × 81, 108 × 108, 135 × 135, 162 × 162, and 189 × 189 μm^2, and a channel length of 5 mm. Microfluidic devices made from the resin TA20 for emulsion formation experiments are designed with channel cross sections of 200 × 200 μm^2 for the continuous phase and cross sections of 100 × 100 μm^2 for the dispersed phase. 3D printing is then performed with the layer thickness set to 25 μm, and an exposure time of 4 s. Uncured resin trapped inside the 3D-printed flow cells is partially removed by immersion and ultrasonication in IPA for several minutes and further immersion in IPA or EtOH until no extraction of Sud1 is observed. Afterward, the inflow ports of the 3D-printed devices are connected to a syringe filled with IPA and flushed several minutes. Finally, the flow cells are postcured for at least 10 min in an Otoflash G171, flushed with IPA again, and dried at air for approximately 1 h before further usage.

2.7. Microfluidic Emulsion Formation. After postprocessing of the 3D-printed microfluidic devices, fine-bore polyethylene tubings (Portex, 380 μm inner diameter) are inserted into the inflow and outflow ports and fixed using a polyolefin glue (Loctite 406/770). To prevent wetting of the aqueous, dispersed phase on the microchannel walls, their hydrophobicity is improved by flushing a solution of (tridecafluoro-1,1,2,2-tetrahydroocyl)-trichlorosilane (0.5% v/v) in HFE-7500 into the microfluidic device, where it is left for several minutes prior to usage. To improve microscopic monitoring of emulsion formation, all microfluidic devices are fixed on a glass slide with a droplet of immersion oil in-between. For microfluidic experiments, water (Milli-Q) is used as dispersed phase, and HFE-7500 with 15% (w/w) of a homemade surfactant based on the ammonium salt of Krytox (FSH) is used as the continuous phase. The flow rates are set to Q_C = 1200 $\mu L\ h^{-1}$ and Q_D = 500 $\mu L\ h^{-1}$. These flow rates first remain constant during water-in-oil (W/O) emulsion formation, whereas the injection volume of the syringe pump connected to the droplet size regulator gradually increases from 0 mm^3 until droplet formation terminates due to microchannel collapse at a volume of >780 mm^3 for the ring regulator and >760 mm^3 for the pliers regulator with an injection rate of 10 000 $\mu L\ h^{-1}$. For a given volume of injected air, emulsion droplets are collected on glass slides multiple times to avoid cross-collection of emulsions formed while switching from one to the next injected air volume level. Diameters of emulsion droplets are evaluated with the software ImageJ based on bright-field microscopy images. Droplet size cycle tests are carried out using the exact same microfluidic chip made from resin TA20.

3. RESULTS AND DISCUSSION

All chemical structures of resin components used for this study are depicted in Figure S1, with POEA being both the monomer and solvent for the other components of the resin formulations. POEA is a low-viscous (7−8 cP at 25 °C), transparent and hydrophobic liquid, which was previously used to form polymer networks with 1,6-hexanediol diacrylate to study its swelling behavior.[56] It already cures fast without the addition of any cross-linker upon UV irradiation, yet yielding mechanically rather unstable polymer structures. Thus, we combine one of three different cross-linkers with POEA in the formulations to form 3D-printable, mechanically more stable objects. The first cross-linker, E8413, is a highly viscous (35 000 cP at 60 °C) cross-linker consisting of an aliphatic urethane diacrylate diluted with 33% (w/w) isobornyl acrylate (IBOA) that are both miscible with POEA. E8413 was already used as a resin component for 3D-printing elastic materials[46,57−60] The second one, TATATO is a triallyl-functionalized cross-linker, which was used in thiolene-based thin-coatings[61,62] and DLP 3D-printing.[63−65] The third one, TPGDA is a low-viscous (15 cP at 25 °C) and transparent bifunctional acrylate, which was used as a base material for material jetting[66] and for 3D printing of microfluidic valves by our group.[43] Formulations consisting of TPGDA usually result in stiff objects, as shown in the preliminary studies of the mechanical properties of three resins containing different fractions of TPGDA and POEA (Figure S2).

3.1. Material Characterization. We start by exploring the polymerization rates of our resin library consisting of six different resin formulations. Each resin contains 0.225% (w/w) photoabsorber Sud1 and 0.1% (w/w) photoinitiator TPO dissolved in POEA and one cross-linker at two different concentrations, adding up to six resin formulations under investigation in total (Table 1).

3.1.1. Polymerization Rates. To determine the layer thickness for a given exposure energy, so-called spot tests (as named by the printer company) are conducted. These spot tests are a useful tool to optimize minimal feature size and reduce resin consumption by predicting layer thicknesses in

Table 1. Resin Formulations with Corresponding Weight Percentages of POEA and the Cross-Linkers E8413, TPGDA, or TATATO[a]

resin formulation	POEA in % (w/w)	cross-linker in % (w/w)
E7.5	92.175	7.5% E8413
E15	84.675	15.0% E8413
TP2.5	97.175	2.5% TPGDA
TP5	94.675	5.0% TPGDA
TA20	79.675	20.0% TATATO
TA40	59.675	40.0% TATATO

[a]Each resin formulation contains 0.1% (w/w) TPO and 0.225% (w/w) Sud1.

https://doi.org/10.1021/acsami.1c05547
ACS Appl. Mater. Interfaces 2021, 13, 31086−31101

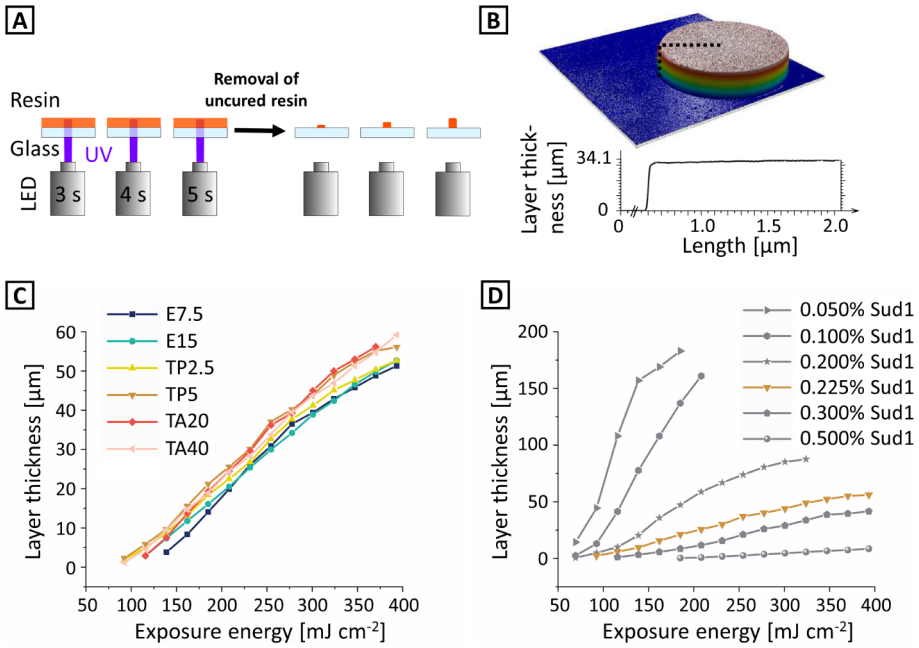

Figure 2. Spot test measurements for evaluating polymerization rates of individual resins. (A) Resin poured onto a glass slide is exposed by defined UV-light spots with a diameter of approximately 1.4 mm generated by the 3D printer LED for different exposure times. After removal of excess resin by flushing with acetone and IPA, (B) confocal microscopy images of cured, dry polymer spots and their height profile are recorded that correspond to the achievable minimal layer thickness in the actual flow cell printing process. (C) Layer thicknesses of the six resins investigated (cf. Table 1) depending on UV-light exposure energy. (D) Layer thicknesses of an exemplary formulation consisting of POEA, 5.0% (w/w) TPGDA, 0.1% (w/w) TPO, and different fractions of Sud1. The brownish plot (stars) is identical with the plot of resin TP5 in (C).

advance to the printing process, especially when resin components are expensive or hardly stable at ambient conditions. A sample of liquid resin is poured onto a glass slide and exposed by the printer's UV lamp with an energy of 46.3 mW cm^{-2} for a certain exposure time (Figure 2A). After the removal of excess resin, the height profile of the cured spot is measured by confocal microscopy (Figure 2B), allowing for extracting the layer thickness depending on the exposure energy in good approximation (Figure 2C,D). Generally, more cross-linker provides more reactive groups (e.g., C−C double bonds) to react toward a dense polymer network, thus producing mechanically more stable and thicker layers of resins.[37] As shown in Figure 2C, the layer thickness of a resin formulation does not vary as significantly as one would expect taking the three different molecular structures of the cross-linkers into consideration (Figure S1). All resins produce rather similar layer thicknesses for exposure energies of 181.8−393.3 mW cm^{-2} with maximum layer thickness deviations of 8 μm. The resins E7.5 and E15 containing E8413 as the cross-linker show slightly lower polymerization rates compared to the other four resins. Although TA20 and TA40 consist of relatively large amounts of TATATO, which—with its three reactive, allyl-bearing moieties—should lead to a densely cross-linked photopolymer and thus higher achievable layer thickness compared to the other four resins, we expect TATATO to be less prominent in the polymerization process due to the intrinsically lower reactivity of allyl groups compared to acrylate groups present in the other two cross-linkers and four resin formulations, respectively.

An additional factor in the process of evaluating the polymerization rate of a resin is the critical exposure energy, which in our case is the lowest energy (multiple of 23.1 mW cm^{-2}) that produces a mechanically stable resin layer. For the resins E7.5 and E15, the critical exposure energies are 138.8 and 115.7 mW cm^{-2}, respectively, thus being higher than for the resins TP2.5 and TP5 (both at 92.5 mW cm^{-2}) as well as for resins TA20 and TA40 (115.7 and 92.5 mW cm^{-2}, respectively). Figure 2D proves that the photopolymerization rate is mainly dictated by the ratio of photoinitiator and photoabsorber rather than the functionality and concentration of the cross-linker in the resin formulation. Here, the addition of only small amounts of Sud1 already induces significant changes in layer thickness, as shown in Figure 2D, where resins containing POEA, 5% (w/w) TPGDA, 0.1% (w/w) TPO, and different weight fractions of Sud1 are screened regarding their polymerization rates. With increasing concentrations of Sud1, the layer thickness decreases, and the critical exposure energy shifts to higher values due to a higher absorption of UV light in the resin. The optimal amount of photoabsorber for 3D-printing microfluidic devices with a minimum layer thickness of 25 μm ranges from 0.2% to 0.3% (w/w). Thus, we choose a concentration of 0.225% (w/w) Sud1 for all further tested photopolymer formulations characterized by a relatively flat curve in the layer thickness/exposure energy plot with achievable layer thicknesses ranging from 2 to 59 μm for exposure energies from 92.5 to 393.3 mW cm^{-2} and a curing onset of 2 to 3 s (92.5−138.8 mJ cm^{-2}) after first exposure. The small slopes in the layer thickness/exposure energy plots ensure easier adjustment of the layer thickness in the 3D-printing process and access to higher resolution in Z direction. For example, if an object is not printed successfully for a given exposure energy per layer, a small increase in the exposure energy can lead to a rather small increase in the layer thickness, which may then be sufficient for a successful print maintaining high resolution without risking an additional, high UV-light penetration into neighboring layers. If the photoabsorber concentration is set to a significantly higher concentration, e.g., 0.5% (w/w), the layer thickness may be adjustable with better

https://doi.org/10.1021/acsami.1c05547
ACS Appl. Mater. Interfaces 2021, 13, 31086−31101

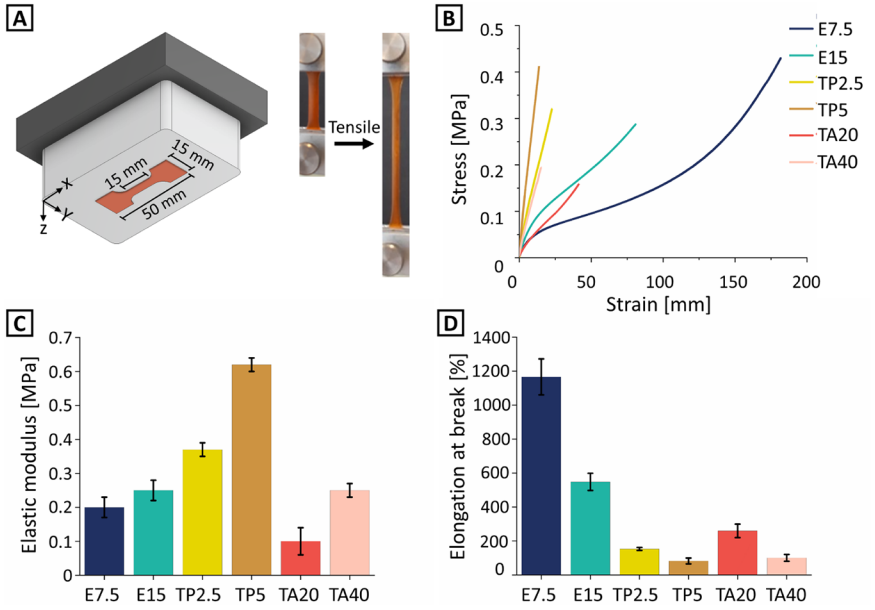

Figure 3. Tensile measurements of six developed resin formulations. (A) Dog bones are 3D-printed in *X*, *Y* plane with a set thickness of 0.5 mm. (B) Exemplary stress−strain curves of PμSL-printed dog bones with respective average tensile stresses at break of $\sigma_{E7.5}$ = 0.38 ± 0.09 MPa, σ_{E15} = 0.24 ± 0.02 MPa, $\sigma_{TP2.5}$ = 0.31 ± 0.02 MPa, σ_{TP5} = 0.36 ± 0.07 MPa, σ_{TA20} = 0.13 ± 0.02 MPa, and σ_{TA40} = 0.18 ± 0.03 MPa. (C) Corresponding elastic moduli are $E_{E7.5}$ = 0.20 ± 0.03 MPa, E_{E15} = 0.25 ± 0.03 MPa, $E_{TP2.5}$ = 0.37 ± 0.02 MPa, E_{TP5} = 0.62 ± 0.02 MPa, E_{TA20} = 0.10 ± 0.04 MPa, and E_{TA40} = 0.25 ± 0.02 MPa ($E_{Sylgard184}$ = 2.4 MPa).[48] (D) For the six investigated resins, elongations at break of 3D-printed dog bones are $\varepsilon_{E7.5}$ = 1167 ± 106%, ε_{E15} = 548 ± 51%, $\varepsilon_{TP2.5}$ = 153 ± 9%, ε_{TP5} = 82 ± 17%, ε_{TA20} = 260 ± 40%, and ε_{TA40} = 101 ± 20% ($\varepsilon_{Sylgard184}$ = 135%).[48]

precision, but the overall 3D-printing process will last longer due to the slower polymerization of each layer. Additionally, the range of feasible layer thicknesses is limited, e.g., one would only be able to print within a certain layer thickness range up to 10 μm as visible for formulation with 0.5% (w/w) Sud1. However, photoabsorber concentrations much lower than the optimal range identified above, like 0.05% (w/w) or 0.1% (w/w), exhibit higher polymerization rates but limit the ability to precisely adjust the layer thickness which may result in less resolved 3D-printed objects. Overall, resins with 0.225% (w/w) Sud1 and 0.1% (w/w) TPO fit well for the 3D printing of objects, and microfluidic devices in particular, with the layer thickness set between 10 and 50 μm, thus providing a balance between high resolution and low printing process times.

3.1.2. Mechanical Properties. In view of the desired 3D-printing of flow cells that provide material elasticity similar to PDMS and that is sufficient to integrate functional elements, we elucidate the mechanical properties of the processed resin library in detail. For that, dog bones 3D-printed in *X*,*Y* plane from all six resin formulations (Figure 3A) are characterized regarding their maximum stress σ, elastic modulus E, and elongation at break ε by tensile tests (Figure 3B−D). Dog bones prepared from resins E7.5 and E15 with E8413 as a cross-linker exhibit E moduli of 0.20 ± 0.03 and 0.25 ± 0.03 MPa with elongations at break of 1166 ± 105% and 548 ± 51%, respectively. Resins TP2.5 and TP5 exhibit elastic moduli of 0.37 ± 0.02 and 0.62 ± 0.02 MPa with elongations at break of 153 ± 9% and 82 ± 17%, respectively. Compared to our previous studies utilizing high amounts of TPGDA (Figure S2) with elastic moduli ranging from 3.9 to 10.2 MPa and elongations at break around 3−4%, the elastic modulus of TP2.5 and TP5 decreases drastically while the elongation at break increases. Despite this significant increase in flexibility, TP5 containing 5% (w/w) TPGDA still yields the highest elastic modulus and the lowest elongation at break among all six developed resins. On the contrary, resin TA20 with TATATO as a cross-linker shows the lowest Young's modulus with 0.10 ± 0.04 MPa and a higher elongation at break than resin TP2.5 and TP5 with 260 ± 40%. Consequently, the material is soft and stretchable but may break easier at higher forces. Resin TA40 with twice the amount of TATATO compared to TA20 shows an increase in elastic modulus and a decrease in elongation at break due to a higher cross-linking density with E = 0.25 ± 0.02 MPa and ε = 101 ± 20%. As discussed previously,[56] POEA—compared to other aromatic monomers (e.g., styrene)—may lead to more flexible polymer networks due to its structure being less rigid. The commercial aliphatic urethane diacrylate (E8413) consists of soft and hard oligomeric or polymeric segments that provide the basis to tune the elasticity of the 3D-printed materials, either by varying the molecular weight or by changing the chemistry of the respective segment.[67] Due to the high ductility of E7.5 and E15, we expect the content of soft domains being more prominent in the aliphatic urethane diacrylate than the hard domains. Furthermore, the hydrogen bonds forming between the amine and carbonyl groups of the aliphatic urethane diacrylate are expected to dissipate energy upon mechanical loading and may also promote the high stretchability of the cured material.[46] For TATATO and TPGDA, both being short-length (or low-molecular) cross-linkers, the resulting polymer network flexibility is generally lower due to the absence of predesigned "soft segments" as in the aliphatic urethane diacrylate E8413. Here, we expect POEA to quickly polymerize and copolymerize with TPGDA and TATATO, respectively, resulting in a network with long PPOEA chains and thus still yielding a ductile material, as observed in the elongations of, e.g., TP2.5 and TA20. With TPGDA being an acrylate and thus, providing faster polymerization upon UV irradiation compared to TATATO (carrying allyl groups), less TPGDA is necessary to yield structures with similar flexibility

https://doi.org/10.1021/acsami.1c05547
ACS Appl. Mater. Interfaces 2021, 13, 31086−31101

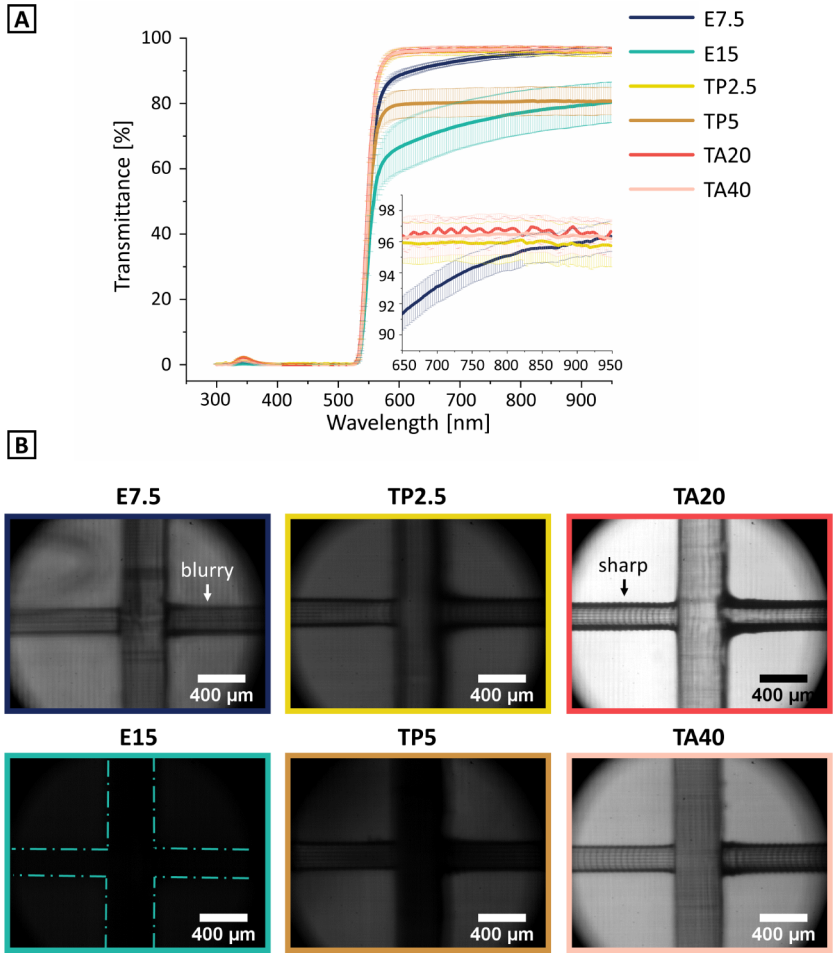

Figure 4. Optical properties of 3D-printed polymer materials made from the resin library developed in this study, and visibility of microchannels within corresponding PμSL-printed flow cells. (A) Transmittance spectra of 3D-printed samples with a designed thickness of 0.5 mm measured at wavelengths from 350 to 950 nm with 3 nm increments. The plot inset highlights the transmittance spectra of E7.5, TP2.5, TA20, and TA40 from 650 to 950 nm. (B) Bright-field microscopy images of microchannel junctions of microfluidic test chips 3D-printed from each resin formulation with identical printing parameters. The frame color depicts the respective resin formulation utilized for the device fabrication and plotted in (A).

as resin 5 (TA20) and resin 6 (TA40). As shown in Figure S2, high amounts of TPGDA result in relatively stiff 3D-printed objects, showing maximum elongations of only approximately 3.5%. We attribute this material property to the higher cross-linking density that can be achieved with TPGDA compared to TATATO. At relatively low fractions of TPGDA (TP2.5 or TP5), it takes less part in the network-forming process and thus the network is less dense owning more flexible character. The flexibility is additionally enhanced due to a fraction of non- or partially polymerized base material inside the 3D-printed product.

To sum this up, the mechanical properties of our formulations vary significantly with elastic moduli ranging from 0.10 ± 0.04 to 0.62 ± 0.02 MPa and elongations at break ranging from 82 ± 17% to 1167 ± 106%. Since TP5 and TA40 exhibit the lowest elongations at break among our six tested formulations (ε_{TP5} = 82 ± 17% and ε_{TA40} = 101 ± 20%), we assign them to be less suitable in terms of resisting high expansions in the later microfluidic application. Also, the two resins exhibit a lower elongation at break than PDMS, with a typical elastic modulus and maximum elongation of Sylgard 184 (10:1) being 2.4 MPa and 135%, respectively.[48]

3.1.3. Optical Properties. For studying processes within microfluidic devices, their optical transmittance and thus the ability to in situ visualize delicate, transient processes, e.g., microdroplet formation, is essential.

Therefore, we determine the transmittance of PμSL-printed samples (Figure 4A) with a target thickness of 0.5 mm fabricated in *X* and *Y* directions (planar to the print head, cf. Figure 3A) as well as 3D-printed test flow cells to evaluate their suitability for monitoring defined flow pattern formation therein (Figure 4B). For all six resins, transmittance is close to zero from 300 to 519 nm due to the strong absorption of Sud1 in that wavelength range, and TPO absorbing from 325 to 415 nm. The formulations TP2.5, TA20, and TA40 yield the highest transmittance in the range of 579−950 nm with values of over 95%. The resins E15 and TP5 show the lowest maximum transmittances of 80% and 81%, respectively. Both resins containing E8413 (E7.5 and E15) do not show constant transmittance starting from 579 nm, as compared to the TPGDA- and TATATO-containing resins, but rather show a steady increase until 950 nm. Therefore, their average transmittance in the visible-light range is significantly lower compared to TP2.5, TA20, and TA40. We expect the scattering and deviations in light absorption—especially visible for the resins E15 and TP5—to originate from small variations in surface roughness and thickness throughout the measured samples. The observed light scattering could further originate

https://doi.org/10.1021/acsami.1c05547
ACS Appl. Mater. Interfaces 2021, 13, 31086−31101

from variations in composition in the amorphous structure as well as the formation of small defects in the material upon increasing the amount of cross-linker for TP5 and E15.

To illustrate the influence of transmittance on the visualization of microstructures within a 3D-printed object, microfluidic devices with a flow-focusing cross-junction and channel dimensions of 400 × 400 μm^2 for the inflow channel of the continuous phase and 200 × 200 μm^2 for the inflow of the dispersed phase are fabricated using identical exposure times, followed by bright-field microscopy characterization (Figure 4B). The thickness of these 3D-printed devices is designed to be 6.5 mm, while the distance from the channel plane to the bottom of the device is designed to be 1.2 mm. Here, microchannels residing inside a 3D-printed flow cell made from TA20 show sharp edges and high contrast as well as the highest transmittance of all 3D-printed devices, also indicated by the brightness of microscopy images (Figure 4B), followed by 3D-printed flow cells made from TA40. In contrast, using the same imaging settings on the same bright-field microscope, the same microchannel cross-junction inside flow cells made from resins such as E7.5, E15, TP2.5, and TP5 appear rather blurry and dark due to lower transmittances compared to TA20. While the TPGDA-containing resins TP2.5 and TP5 show significant dimming and blurring effects that render monitoring of droplet formation a rather challenging task, the measured transmittances of 3D-printed samples made from TP2.5, and also TA40, appear higher than the images of the flow devices (Figure 4B) suggest, compared to TA20. We attribute this to the difference in printing direction of the corresponding sample type, where the microchannels of the flow cells have been 3D-printed perpendicular to the *X*, *Y* plane to ensure sufficient resolution of the droplet channel, while the transmittance samples are 3D-printed in parallel to the *X*, *Y* plane due to the small sample thickness. With 3D-printed parts made from E15 displaying the lowest average transmittance in the visible range and the poorest imaging of the microchannel cross-junction, it is also the least appropriate for the desired microfluidic application. Although E7.5 and TP2.5 also exhibit blurring and dimming, the effect is less apparent than in, e.g., E15 and TP5, and monitoring of emulsions should still be manageable. Thus, at this point, resins E7.5, TP2.5, and TA20 seem most suitable for the design of microfluidic devices, also taking the previously discussed mechanical properties into account.

3.1.4. Resin Viscosity and Minimum Feature Size. In addition to the previous parameters (layer thickness, mechanical, as well as optical properties), the successful processing of resins via PμSL into micrometer-resolved polymer materials also depends on the resin's viscosity. Low-viscous formulations are advantageous for fabricating parts with small internal features such as microchannels due to faster liquid drainage out of the fabricated channel voids, reducing the occurrence of clogging. Moreover, removing uncured resin residing in the channel edges after the printing process with air or solvents is simplified, rendering the postprocessing of 3D-printed objects less error-prone and faster.

However, adding neat E8413 cross-linker—being highly viscous at room temperature—to the POEA-based photopolymer formulations increases the viscosity, studied at shear rates of 1−1000 s^{-1} (Figure S3A), significantly in case of E7.5 (32 cP) and E15 (91 cP), as compared to a viscosity of neat POEA of 7−8 cP. The addition of TATATO to POEA also increases the viscosity to 13.4 and 19.1 cP for TA20 and TA40, while viscosities of TP2.5 and TP5 upon the addition of TPGDA are 8.3 and 8.4 cP, respectively. Since the viscosity of all investigated resins is low compared to common commercial resins that are designated for high-resolution 3D printing, e.g., Perfactory R11 (Envisiontec, Gladbeck, Germany) with a viscosity of approximately 500 cP,[33] we should not observe significant differences in achievable minimal feature size among our resin formulations.

To test this hypothesis, we 3D-print cubic objects with identical printing parameters for the prescreened resins E7.5, TP2.5, and TA20, which exhibit the lowest cross-linker content and thus the lowest viscosity for each of the three different cross-linkers. The cross-sections of the internal microchannels are chosen to be multiple integers of the 3D printer's pixel size (54, 81, and 108 μm). For the resins E7.5 and TP2.5, only microchannels with a desired cross-section of 81 and 108 μm are obtained (Figure S3B). As uncured E8413—used for preparing resin E7.5—is more challenging to remove during postprocessing and also tends to precipitate as a whitish solid upon flushing with common polar solvents such as IPA or EtOH, E7.5 is less suited for microfluidic device fabrication with low internal feature sizes. Even if one may use less polar solvents like acetone for postprocessing to circumvent precipitation, our 3D-printed parts show swelling (cf. Figure S5), thus users may unintentionally change the microchannel's aspect ratio or even permanently damage the microchannel structure. In contrast to the above-discussed results for the resins E7.5 and TP2.5, all three types of microchannels (54, 81, and 108 μm cross-sections) inside TA20-based objects are successfully printed and can be flushed with IPA during postprocessing (Figure S4A).

Considering all previously discussed aspects like mechanical and optical properties as well as resolution and postprocessability, we choose to move forward with resin TA20 for microfluidic device fabrication.

3.1.5. Minimum Internal Feature Sizes and Solvent Stability of 3D-Printed Parts Made of Resin TA20. Since bright-field microscopy provides rather limited information about microchannel dimensions in a 3D-printed object, we conduct SEM measurements. For that, cubic flow cells with parallelly aligned microchannels (54 × 54, 81 × 81, 108 × 108, 135 × 135, 162 × 162, and 189 × 189 μm^2) are fabricated at a set layer thickness of 25 μm (Figure 5A).

The 3D-printed device is then cut into two pieces perpendicular to the microchannels and imaged by SEM on the cut-open surface to determine the individual microchannel's cross-sections (Figure 5B). The cross-section of the channel designed to be 54 × 54 μm^2 is more circular than square with dimensions of approximately 35 × 46 μm^2 (Table 2). The channel envisioned to be 81 × 81 μm^2, is 9 × 9 μm^2 smaller in practice. Although the dimensions for the microchannel designed to be 108 × 108 μm^2 are nearly identical to the printed channel (106 × 106 μm^2), with increasing design dimensions, this deviation shifts toward higher positive values for the following three channels, with the largest channel designed to be 189 × 189 μm^2 showing a deviation of additional 34 × 42 μm^2. Corresponding SEM images recorded at an angle 45° as well as bright-field microscopy images of the squared channels are depicted in Figure S4. The fact that common 3D-printed flexible materials barely offer feature sizes of 100 μm or lower even for 3D-printed structures just open to air renders the above-shown results unique for PμSL-printed flexible materials.

https://doi.org/10.1021/acsami.1c05547
ACS Appl. Mater. Interfaces 2021, 13, 31086−31101

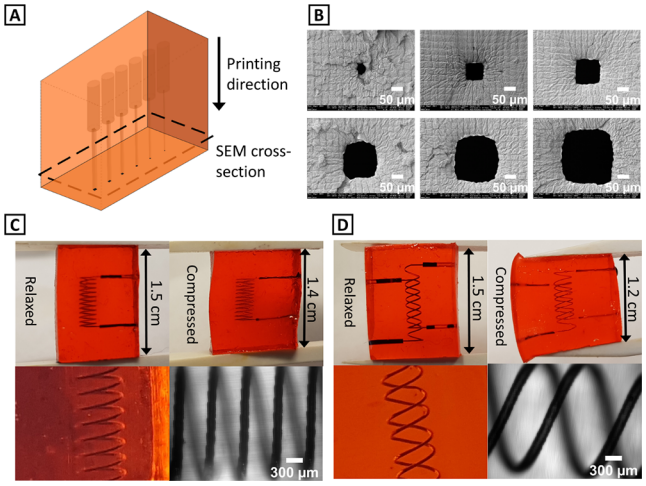

Figure 5. Minimal feature size of flexible microfluidic devices PμSL-printed with resin TA20, and testing of achievable 3D geometric complexity. (A) Schematic of test object with integrated microchannels being 54 × 54, 81 × 81, 108 × 108, 135 × 135, 162 × 162, and 189 × 189 μm^2 in diameter. For SEM measurements, the corresponding 3D-printed part is cut into two pieces to examine the size of microchannel cross-sections inside. (B) Corresponding SEM images. (C and D) Visualization of material flexibility of 3D-printed flow cells made from resin TA20. To improve their visibility, microchannels inside 3D-printed parts in (C) and (D) are filled with an aqueous solution of Brilliant black dye, and the flow cell is coated with immersion oil. (C) Single-coiled and (D) double helix-like microchannels with a circular diameter (top view) of approximately 200 μm and the respective bright-field microscopy image (bottom row, right).

Table 2. Internal Channel Cross-Sections Designed to Multiple Integers of 27 × 27 μm^2 (Pixel Size) with a Channel Length of 5 mm and Their Respective Dimensions Determined by SEM

design (μm^2)	SEM measurement (μm^2)	deviation (μm^2)
54 × 54	35 × 46	−19/−8
81 × 81	72 × 72	−9/−9
108 × 108	106 × 106	−2/−2
135 × 135	147 × 150	+12/+15
162 × 162	188 × 197	+26/+35
189 × 189	223 × 231	+34/+42

To demonstrate that the high resolution of TA20 for inner void structures is not only feasible for straight, square microchannels but also for more complex geometries,[32] we 3D-print an inner-laying coil (Figure 5C) as well as a double-helix structure (Figure 5D). Thus, we expect the resin TA20 to be applicable for more complex microchannel geometries and applications, as discussed in the next chapters.

To assess the applicability of microfluidic devices made from resin TA20, we also perform swelling studies in different solvents exposing PμSL-printed discs made from TA20 with a diameter of 10 mm and a thickness of 1 mm for 1, 3, and 24 h to water (MilliQ), IPA, EtOH, DMSO, THF, toluene, *n*-hexane, and HFE-7500 (Figure S5). The discs significantly swell in DMSO, THF, and toluene within 1 h, hardly in polar protic solvents such as water, IPA, and EtOH, and we do not observe any swelling in nonpolar solvents like *n*-hexane and HFE-7500 even after 24 h. As only a slight yellowish coloring by Sud1 in the supernatant HFE-7500 is visible after 3 h, TA20-based flow cells exhibit proper solvent resistance, particular for one of the key experiments in microfluidics, which is emulsion formation from HFE-7500 and water.[68,69]

Additionally, to visualize the changes upon UV irradiation in our resin, FTIR measurements of TA20 before and after UV polymerization are conducted (Figure S6). Here, we spot three significant bands potentially providing information on the structural changes upon UV polymerization. The first band at approximately 3083 cm^{-1} refers to CH_2 stretching of the allyl group of TATATO that is only visible in the pure TATATO spectrum.[65] In the UV-polymerized sample, the band is overlapping with aromatic C—H bands from POEA as well as vibrations of the CH_2 stretches of the vinyl group and the $-CH_2$ group. Thus, this band and changes of it cannot be easily identified in the UV-cured sample. The second band at 1637 cm^{-1} referring to vibrations of C═C stretching of POEA overlaps with vibrations of C═C stretching of the allyl group of TATATO, that generally shows a high absorption coefficient in the IR spectrum.[56] Here, a small shoulder at approximately 1640 cm^{-1} is still visible in the UV-cured sample, indicating that the double bond of the allyl group is not fully consumed. The third band of interest is at 808 cm^{-1} and refers to the ═CH_2 twist of double bonds in POEA. Here, a decrease in band intensity is visible indicating the curing of POEA and the reduction of double bonds within the resin. Since the band is still visible after curing, we conclude that the double bonds of POEA are not fully converted.

3.2. 3D-Printed, Flexible Polymer Micromaterials for Functional Microfluidics. To explore the unique combination of material properties of our best-candidate resin, we implement two flow cell designs, whose functionality is based on compressing the outflow channel shortly behind a droplet-forming microchannel cross-junction to manipulate its cross section and with that regulate the size of emulsion droplets that form at the junction. For that, air pressure is applied via a syringe pump to a microchannel closely surrounding the outflow channel. The first microchannel design of such a droplet size regulator is comprised of a ring-like microchannel fully surrounding the outflow channel with an inner diameter of 0.95 mm, an outer diameter of 1.55 mm, and a thickness of 0.4 mm. The ring-shaped channel is connected to an in-/outflow channel with the dimensions of 4, 0.6, and 0.4 mm (height, width, and length) yielding a total regulator channel volume of 1.4 mm^3 (Figure S7A). A tubing with an inner diameter of 380 μm is cut at a length of approximately 40.7 cm resulting in an overall volume of the air-pressurized droplet regulator of approximately 47.5 mm^3. The ring-shaped channel uniformly surrounds the emulsion-carrying outflow channel at a distance of 375 μm.

While the advantage of a ring-shaped regulator would lie in its capability to uniformly compress the droplet-transporting channel behind the junction from all sides, which should yield a more uniform and stable droplet formation, it may desirable to directly monitor droplet formation at the cross-junction to precisely control flow rate ratio and regulator actuation. On this account, the second regulator design consists of two curved microchannels that are connected to one inflow channel compressing the droplet channel after the junction from the left and right side such that the flow cell junction's top and bottom is not covered by any surrounding microchannel. This should allow better monitoring of the junction area where emulsion droplets are formed. The theoretical volume of these pliers-shaped channels inside the microfluidic

https://doi.org/10.1021/acsami.1c05547
ACS Appl. Mater. Interfaces 2021, 13, 31086−31101

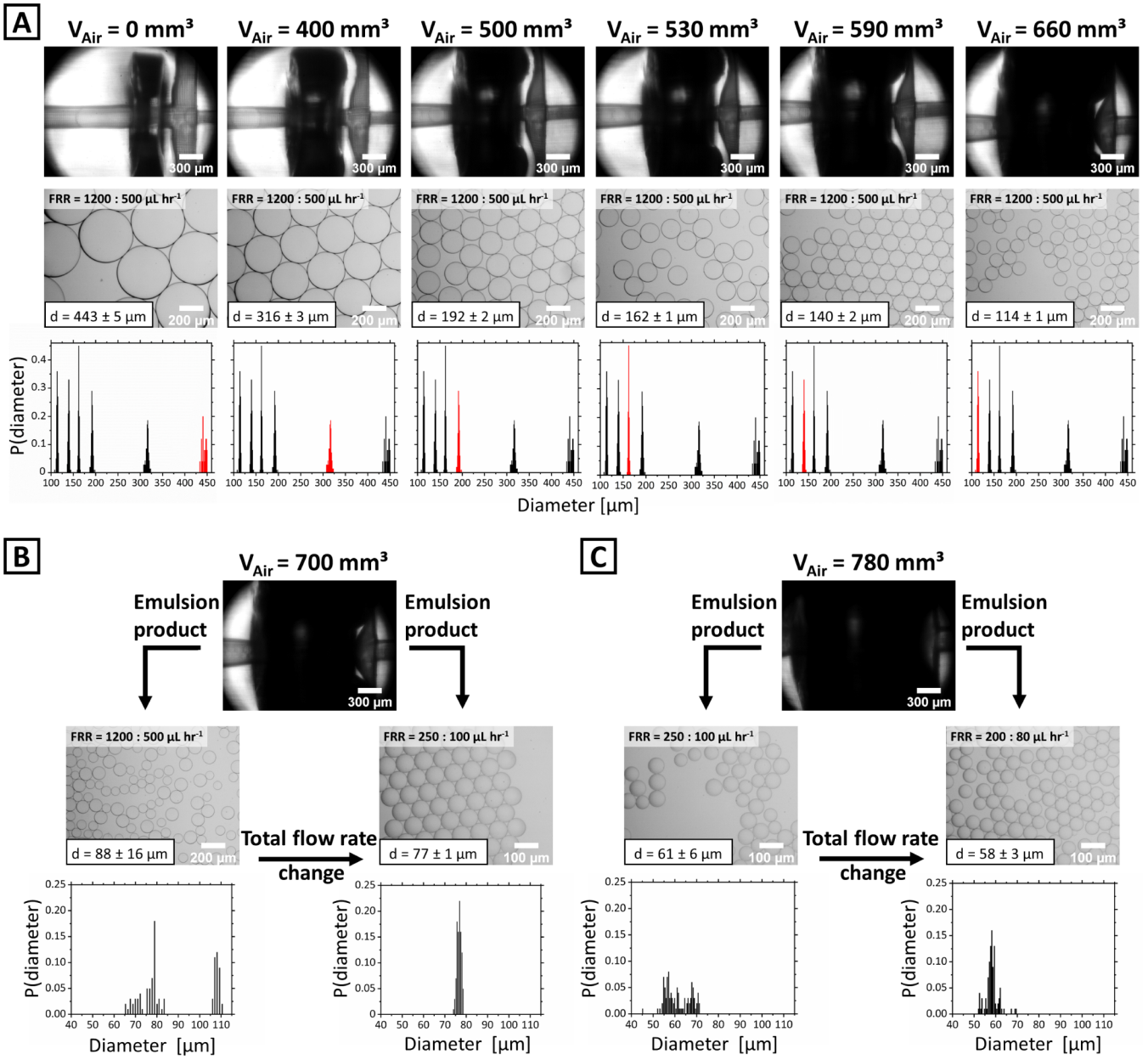

Figure 6. Emulsion formation in a ring-shaped droplet regulator. (A) The regulator is filled with air volumes of 400, 500, 530, 590, and 660 mm^3 at a flow rate of 1200 $\mu L\ h^{-1}$ for the continuous phase and 500 $\mu L\ h^{-1}$ for the dispersed phase. Upper row: images recorded at the junction area; the expansion of the regulator unit is visible. Middle row: Exemplary images of the emulsion products collected for a given expansion. Lower row: histograms of corresponding emulsion products (red). The number of droplets, which have been used for diameter evaluation, are (from left to right) N = 25, 70, 100, 100, 100, and 100. (B) At an injected air volume of V_{Air} = 700 mm^3, nonuniform droplets form (left). Changing the flow ratio from 1200:500 $\mu L\ h^{-1}$ (Q_C:Q_D) to 250:100 $\mu L\ h^{-1}$ (Q_C:Q_D) reduces the standard deviation from ±16 to ±1 μm (right). (C) At an injected air volume of V_{Air} = 780 mm^3, nonuniform droplets are again observed at a flow ratio of 250:100 $\mu l\ h^{-1}$ (Q_C:Q_D). By further adjusting the flow ratio to 200:80 $\mu L\ h^{-1}$ (Q_C:Q_D), the droplet size decreases from 61 ± 6 to 58 ± 3 μm.

device is 5.1 mm^3, yielding an overall regulator volume of approximately 51 mm^3 considering the additional tubing (46 mm^3) for connecting the droplet size regulator with the air reservoir. The dimensions of the pliers-shaped design are depicted in Figure S7B. For both designs, the dimensions of the continuous-phase channel are 200 × 200 and 100 × 100 μm^2 for the dispersed phase.

3.2.1. Ring-Shaped Droplet Regulator. For testing the microfluidic droplet regulator during water-in-oil (W/O) emulsion formation, we set the flow rates for the continuous oil phase to Q_C = 1200 $\mu L\ h^{-1}$ and for the dispersed aqueous phase to Q_D = 500 $\mu L\ h^{-1}$ for all experiments, yielding droplets with an average diameter of 443 ± 5 μm (Figure 6A). As soon as air is injected into the regulator at a flow rate of 10 000 $mm^3\ h^{-1}$, the ring-shaped channel expands, slowly compressing the droplet-forming channel. Initially, at an injected air volume of V_{Air} = 400 mm^3, we observe a reduction of droplet diameter to 316 ± 3 μm. By subsequently expanding the regulator further, monodisperse aqueous droplets with diameters of 192 ± 2 μm (V_{Air} = 500 mm^3), 162 ± 1 μm (V_{Air} = 530 mm^3), 140 ± 2 μm (V_{Air} = 590 mm^3), and 114 ± 1 mm^3 (V_{Air} = 660 mm^3) are obtained.

https://doi.org/10.1021/acsami.1c05547
ACS Appl. Mater. Interfaces 2021, 13, 31086−31101

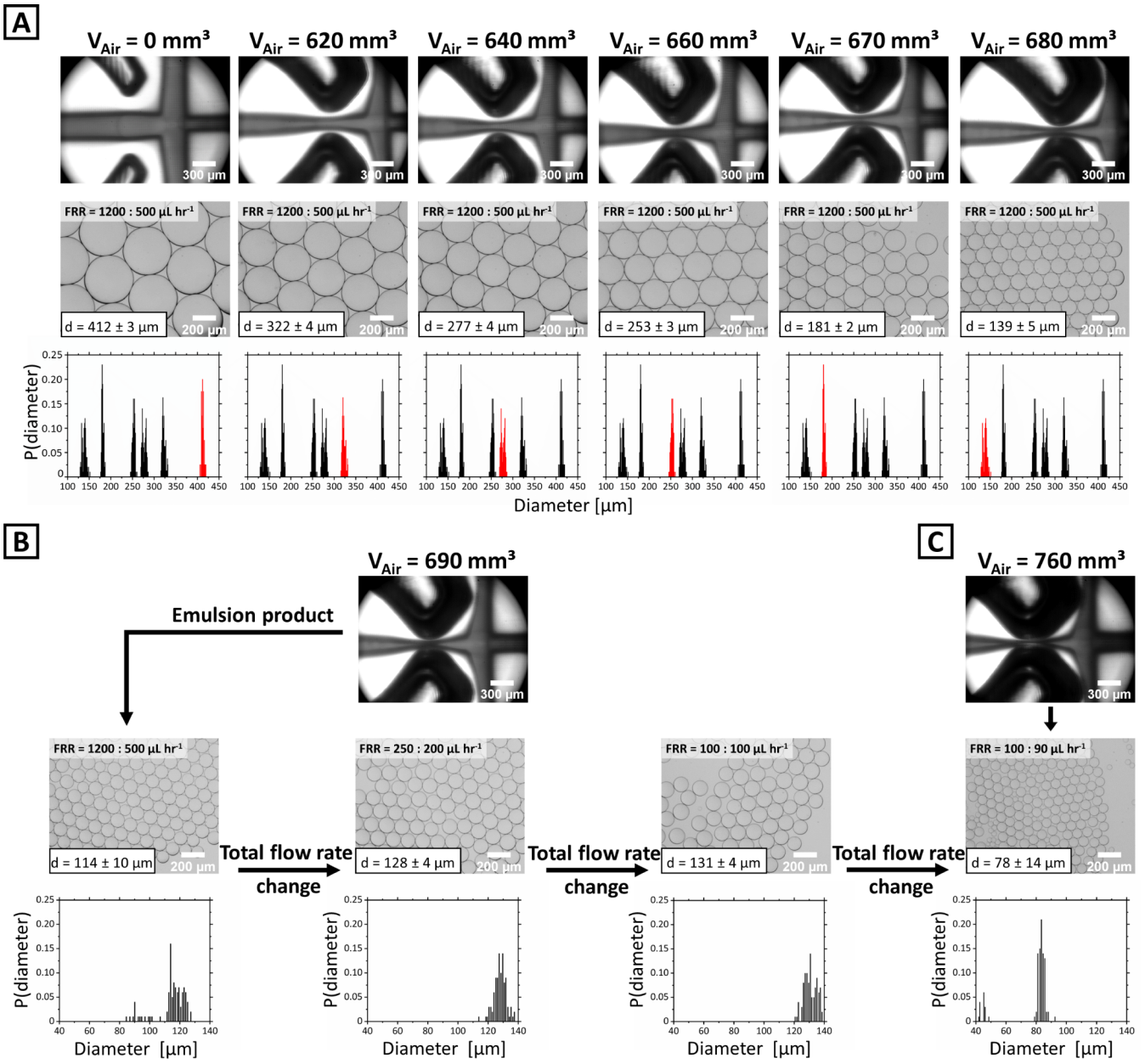

Figure 7. Emulsion formation in a pliers-shaped droplet regulator. (A) The pliers-shaped regulator is filled with air volumes of 620, 640, 660 (identical with cycle 5 in Figure S8), 670, and 680 mm^3 at a flow rate of 1200 $\mu L\ h^{-1}$ for the continuous phase and 500 $\mu L\ h^{-1}$ for the dispersed phase. Upper row: images recorded at the junction area; the expansion of the regulator unit is visible. Middle row: Exemplary images of the emulsion products for a given regulator expansion. Lower row: histograms of corresponding emulsion products (red). The number of droplets, which have been used for diameter evaluation, are (from left to right) N = 40, 80, 100, 100, 100, and 100. (B) At an injected air volume of V_{Air} = 690 mm^3, nonuniform droplets form (left). Changing the flow ratio from 1200:500 $\mu L\ h^{-1}$ (Q_C:Q_D) to 250:200 $\mu L\ h^{-1}$ (Q_C:Q_D) reduces the standard deviation from ±10 μm (left) to ±4 μm (middle). Flow ratio adjustment to 100:100 $\mu L\ h^{-1}$ (Q_C:Q_D) does not reduce the droplet diameter's standard deviations obtaining droplet diameters of 131 ± 4 μm. (C) Eventually, at V_{Air} > 760 mm^3, we obtain even smaller emulsion droplets but with significant standard deviation (78 ± 14 μm).

However, at V_{Air} = 700 mm^3, droplet formation becomes instable resulting in nonuniform emulsion droplets with an average diameter of 88 ± 16 μm (Figure 6B). By changing the flow rates from 1200 and 500 $\mu L\ h^{-1}$ (Q_C and Q_D) to 250 and 100 $\mu L\ h^{-1}$, respectively, we again transition into a stable dripping regime with emulsion droplets being 77 ± 1 μm in diameter. While further expansion of the ring-shaped regulator to V_{Air} = 780 mm^3 again leads to instable droplet formation (Figure 6C), reducing the flow rates to 200 and 80 $\mu L\ h^{-1}$ (Q_C and Q_D) once more results in stable droplet formation, being 58 ± 3 μm in diameter for a microchannel cross section of 200 × 200 μm^2. Further expansion of the regulator eventually causes a collapse of the droplet-forming microchannel.

We assume that adapting the flow rates at high expansions of the pressurized droplet size regulator is necessary due to the increasing compression and collapse of the droplet-forming microchannel creating a high internal pressure. By reducing the flow rates of both emulsion-forming phases at extreme microchannel deformation, the internal pressure is reduced and both, a stable flow pattern and emulsion formation is

https://doi.org/10.1021/acsami.1c05547
ACS Appl. Mater. Interfaces 2021, 13, 31086−31101

restored. The formation of nonuniform emulsion droplets at strong channel compression also lies in the increased contact area of the aqueous phase with the walls of the outflow channel causing undesired wetting and exacerbates droplet encapsulation in the surrounding oil phase. It is also worth mentioning that expansion of the ring-shaped regulator and therefore reduction of the droplet-forming channel cross-section at constant flow rates Q_D and Q_C leads to a significant increase in droplet formation frequency (Movie 1 and Movie 2). To investigate the reproducibility of droplet size regulation, we conduct cycle tests using the same microfluidic device with integrated ring-shaped regulator and repeatedly inject and withdraw V_{Air} = 590 mm^3 (Figure S8). The obtained droplet diameters after first injection (Cycle 1) are d_{Cycle1} = 149 ± 2 μm and show a deviation of 9 μm compared to the previous microfluidic experiment where V_{Air} = 590 mm^3 yields emulsions with 140 ± 2 μm in diameter. Emulsion droplets obtained after repeated injection and withdrawal of V_{Air} = 590 mm^3 for four more cycles exhibit overall constant diameters of d_{Cycle2} = 149.3 ± 1.1 μm, d_{Cycle3} = 149.1 ± 1.4 μm, d_{Cycle4} = 148.6 ± 1.4 μm, and d_{Cycle5} = 150.1 ± 1.4 μm, indicating good reproducibility of droplet sizes.

3.2.2. Pliers-Shaped Droplet Regulator. As the above-described droplet size regulator fully surrounds the microchannel area of interest due to its ring-like structure, we also utilize a design that provides similar control over a wide range of droplet sizes, but does not obstruct the view into the droplet-forming microchannel junction. This very design is a modification of Abate's valve design for planar PDMS-based microfluidic devices that we adapt for 3D-printed nonplanar microfluidic devices (Figures 7 and S7B). Two channels are designed in a pliers-shaped manner with an angle of 75° toward the plane of microchannels responsible for droplet formation. The tips of both curved channels are located in plane of the droplet-forming microchannel with a distance of approximately 250 μm to the respective droplet-transporting channel edges, and a distance of approximately 260 μm to the channel edges of the continuous phase. As for the ring-shaped droplet regulator, the pliers-shaped design only requires one syringe pump for controlling the injected air volume. As in the former set of emulsion formation experiments, we set the flow rates to 1200 μL h^{-1} for the continuous phase and 500 μL h^{-1} for the dispersed phase for all following experiments. We start with a cycle test to repeatedly inject and withdrawal V_{Air} = 660 mm^3 (Figure S8), causing the average diameter of aqueous droplets to increase from d_{Cycle1} = 226.4 ± 4.8 μm obtained in the first actuation cycle to d_{Cycle2} = 244.2 ± 3.9 μm. In three consecutive cycles, droplets with a diameter of d_{Cycle3} = 250.7 ± 3.6 μm, d_{Cycle4} = 245.2 ± 3.0 μm, and d_{Cycle5} = 253.0 ± 2.9 μm are obtained. On this account, we conclude that the reproducibility of the ring-shaped regulator is better than for the pliers-shaped regulator. Not only is the maximum difference of droplet diameters within the last four cycles with approximately 9 μm for the pliers-shaped design significantly larger than for the ring-shaped regulator design (approximately 2 μm) but also are the diameter's standard deviations for each cycle higher in case of the pliers-shaped droplet size regulator. Next, we investigate the minimum achievable droplet size for the pliers-shaped design (Figure 7A). Without expanding the regulator unit, an average droplet diameter of 412 ± 3 μm is obtained. By increasing the amount of air injected, average droplet sizes of 322 ± 4 μm (V_{Air} = 620 mm^3), 277 ± 4 μm (V_{Air} = 640 mm^3), 181 ± 2 mm (V_{Air} = 670 mm^3), and 139 ± 5 μm (V_{Air} = 680 mm^3) are obtained, indicating that the pliers-shaped design requires high-precision injection of air, as minor expansions already lead to a significant reduction in droplet diameters. However, at V_{Air} = 690 mm^3 injected into the droplet regulator, only nonuniform droplets are obtained (Figure 7B) similar to previous experiments with the ring-like regulator design. By re-adjusting the flow rates to 250 and 200 μL h^{-1} (Q_C and Q_D), again, uniform aqueous emulsion droplets with a diameter of d = 128 ± 4 μm are collected. Further decreasing the flow rates to 100 μL h^{-1} for both the dispersed and continuous phase does not reduce the droplets diameter deviations. Expansion of the pliers-shaped regulator by injecting V_{Air} = 760 mm^3 eventually leads to satellite droplet formation with average emulsion diameters of d = 74 ± 14 μm, where further adjustment of flow rates does not lead to the restoral of a stable flow pattern (Figure 7C). Again, an increase in emulsion throughput upon regulator expansion is again observed (see Movie 3 and Movie 4).

Although the onset of droplet size change upon regulator actuation is observed at significantly higher air volume injected into the pliers-shaped regulator compared to the ring-shaped regulator (V_{Air} = 600 mm^3 compared to V_{Air} = 400 mm^3), the expansion of the pliers-like design seems to have more impact on the droplet's size change after a certain expansion is reached, in this case at V_{Air} = 620 mm^3. We attribute these observations to the nonuniform compression of the droplet channel in case of the pliers-shaped regulator design from two sides in comparison to the uniform compression from all sides using the ring design. To visualize the difference in the compression profile, we design flow cells with similar dimensions of the two designs to monitor the cross section of the droplet channel upon expanding either of the droplet regulators. As bright-field microscopy images imply (Figure S9), the deformation of the droplet channel by expanding the ring-shaped regulator proceeds in a rather uniform manner, where the channel maintains its rectangular shape, and only small changes in the aspect ratio are visible, even at expansions greater than V_{Air} = 700 mm^3 (Figure S9A). In comparison, the droplet-forming channel shape changes significantly from a rectangular to rather ellipsoidal at high expansions of V_{Air} = 700 mm^3 for the pliers design (Figure S9B).

4. CONCLUSIONS

In this work, we designed highly stretchable polymer materials with micrometers resolution by additive manufacturing based on PμSL utilizing a commercial 3D printer. For that, we developed a library of resins that were characterized regarding their photopolymerization rates, mechanical properties, optical properties, and viscosities. Layer thicknesses from 5 to 60 μm (corresponding to an UV-irradiation energy of 92.5 to 393.3 mJ cm^{-2}) were achieved, thus covering the exact minimal feature size range of established microfluidic device fabrication, with transmittances ranging from 80% to 97%, and E moduli ranging from 0.10 to 0.62 MPa. Eventually, a resin consisting of POEA, 20% (w/w) TATATO, 0.1% (w/w) TPO, and 0.225% (w/w) Sud1 was further utilized for fabricating flexible microfluidic devices via PμSL due to its superior properties over all other tested resins regarding transmittance, minimal microchannel features of approximately 35 × 46 μm^2, and resistance toward commonly used solvents in microfluidics, e.g., water or fluorinated oils. In combination with its desirable mechanical properties, the resin was utilized for PμSL-printing

https://doi.org/10.1021/acsami.1c05547
ACS Appl. Mater. Interfaces 2021, 13, 31086−31101

flexible flow cells for microemulsion formation with integrated, air-filled microchannels that could expand and shrink, leading to a compression of the droplet-forming cross-junction and thus, reduction of emulsion droplet sizes. We show that monodisperse droplets with diameters ranging from 443 ± 5 to 58 ± 3 μm were achieved for a ring-shaped regulator, and droplets with diameters of 412 ± 3 to 128 ± 4 μm were achieved for a pliers-shaped regulator. Droplet sizes did not change significantly for five tested cycles utilizing the ring-shaped regulator design. That very design is superior over the pliers-shaped regulator in terms of lowest achievable and monodisperse droplet size, which we expect to arise from the all-around, uniform channel compression.

Our work provides access to integrated microfluidic devices with tunable mechanical properties based on commercially available 3D printing and easy-to-prepare, likewise commercially available starting materials. As-fabricated flow cells are able to compete with PDMS-based microfluidics in terms of material properties (optical transparency, flexibility, and minimal feature size) and applicability to tailor fluid flow and emulsion formation on demand. Thus, 3D-printed droplet size regulators are particularly useful for microfluidics users who neither want to invest in multiple devices for conventional flow cell fabrication nor proceed through iterations of device design and optimization. Nonetheless, we plan on further optimizing our approach toward functional, elastic PμSL-printed microflow cells. For instance, a decrease of transmittance was observed upon flushing the microfluidic devices with a solution of 0.5% (v/v) (tridecafluoro-1,1,2,2-tetrahydroocyl)-trichlorosilane in HFE-7500 to improve the microchannel's hydrophobicity.[70] Thus, we currently focus on the design of more hydrophobic resins that are both flexible and provide micron-scale resolution. To tune the surface properties of our final resin composition, the next logical step will be to incorporate either more hydrophobic compounds (e.g., fluorinated acrylates)[21] or more hydrophilic compounds (e.g., acrylic acid) depending on the desired emulsion type (water-in-oil or oil-in-water) to reduce the amount of potential wetting inside the microfluidic chip design. Here, contact angles at the surface of the outflow channel of >100° (for W/O emulsions) or near to 0° (for O/W emulsions) would be desirable. We expect another improvement by utilizing a high-precision pump with a pressure controller to automatically adjust potential pressure loss or pressure variations during droplet formation, ensuring constant product quality during hours- or even days-long experiments. Although, we successfully show the formation of microemulsions within a wide range of droplet sizes, there are further studies necessary to expand the applications of our microfluidic devices, e.g., studies on producing microgel systems from droplet templates as well as assessing flow cell biocompatibility and long-term stability. Nonetheless, our study not only provides new material combinations for PμSL yielding highly resolved structures inside 3D-printed parts that could be also applied in the field of soft robotics, but also translating an original design solution for manipulating emulsion sizes into 3D-printed, flexible flow cells.

■ ASSOCIATED CONTENT

Supporting Information

The Supporting Information is available free of charge at https://pubs.acs.org/doi/10.1021/acsami.1c05547.

The supporting information file includes the chemical structures of the utilized materials for 3D printing (Figure S1); tensile measurements of resin formulations consisting of POEA and 30% (w/w), 50% (w/w), and 70% (w/w) TPGDA (Figure S2); viscosity measurements of the six presented resin formulations as well as bright-field microscopy images of 3D-printed internal channels made of TP2.5 and E7.5 (Figure S3); SEM images of rectangular channels acquired at an angle of 45° as well as microscopic images of the 3D-printed channels of resin TA20 (Figure S4, cf. Figure 5); changes of discs made of TA20 upon immersion in different solvents (Figure S5); FTIR spectra of TATATO, POEA, TA20, and UV-polymerized TA20 (Figure S6); CAD files of both microfluidic devices utilized for emulsion formation (Figure S7); a graph on emulsion droplet changes upon five cycles of expansion and contraction of the regulator units (Figure S8); microscopic cross-sectional views of both flow cell outlines and visualization of channel contraction upon expansion of the regulator units (Figure S9); and a comparison between obtained minimal resolution in microfluidic devices published in recent years (Table S1) (PDF)

Furthermore, four movies of microfluidic experiments are supplied: Droplet diameter change upon expansion of the ring-shaped regulator focusing on the tubing. Flow rates for the continuous oil phase are set to 1200 μL h^{-1} and for the dispersed aqueous phase to 500 μL h^{-1}. Droplet sizes change (visible in outflow tubing) while the ring-shaped regulator expands (not visible) at the droplet-forming junction (Movie 1) (MP4); Droplet diameter change upon expansion of the ring-shaped regulator focusing on the junction. Flow rates for the continuous oil phase are set to 1200 μL h^{-1} and for the dispersed aqueous phase to 500 μL h^{-1}. While the ring-shaped regulator expands at the droplet-forming junction, droplet diameters change (Movie 2) (MP4); Droplet diameter change upon expansion of the pliers-shaped regulator focusing on the tubing. Flow rates for the continuous oil phase are set to 1200 μL h^{-1} and for the dispersed aqueous phase to 500 μL h^{-1}. Droplet sizes change (visible in outflow tubing) while the pliers-shaped regulator expands (not visible) at the droplet-forming junction (Movie 3) (MP4); Droplet diameter change upon expansion of the pliers-shaped regulator focusing on the junction. Flow rates for the continuous oil phase are set to 1200 μL h^{-1} and for the dispersed aqueous phase to 500 μL h^{-1}. While the pliers-shaped regulator expands at the droplet-forming junction, droplet diameters change (Movie 4) (ZIP)

■ AUTHOR INFORMATION

Corresponding Author

Julian Thiele − *Leibniz Institut für Polymerforschung Dresden e.V., 01069 Dresden, Germany;* orcid.org/0000-0001-5449-3048; Phone: +49-351-4658492; Email: thiele@ipfdd.de

Authors

Niclas Weigel − *Leibniz Institut für Polymerforschung Dresden e.V., 01069 Dresden, Germany*

Max J. Männel − *Leibniz Institut für Polymerforschung Dresden e.V., 01069 Dresden, Germany*

Complete contact information is available at: https://pubs.acs.org/10.1021/acsami.1c05547

Author Contributions

The manuscript was written through contributions of all authors. All authors have given approval to the final version of the manuscript.

Funding

This research was funded by the Federal Ministry of Education and Research (BMBF, Biotechnology2020+: Leibniz Research Cluster, 031A360C), the Volkswagen Foundation ("Experiment!"), and the German Research Foundation (DFG, Research Training Group 1865: Hydrogel-based Microsystems). This project has received funding from the European Research Council (ERC) under the European Union's Horizon 2020 research and innovation program (grant agreement no. 852065).

Notes

The authors declare no competing financial interest.

■ ACKNOWLEDGMENTS

The authors thank Holger Scheibner and Dr. Konrad Schneider for tensile measurements. The authors also thank Michael Göbel and Dr. Peter Formanek for supplying the SEM images. They also thank Dr. Mikhail Malanin for conducting FTIR analysis. Furthermore, they thank Nicolas Hauck, Thomas Heida, Dr. Carola Graf, and Tony Köhler for the critical and fruitful discussions concerning experimental procedures and manuscript preparation (all Leibniz IPF Dresden). Additionally, the authors thank Martin Schumann (TU Dresden) for designing the table of contents graphic.

■ REFERENCES

(1) Friend, J.; Yeo, L. Fabrication of Microfluidic Devices using Polydimethylsiloxane. *Biomicrofluidics* **2010**, *4*, No. 026502.

(2) Golberg, A.; Linshiz, G.; Kravets, I.; Stawski, N.; Hillson, N. J.; Yarmush, M. L.; Marks, R. S.; Konry, T. Cloud-Enabled Microscopy and Droplet Microfluidic Platform for Specific Detection of *Escherichia Coli* in Water. *PLoS One* **2014**, *9*, No. e86341.

(3) Gu, S.; Lu, Y.; Ding, Y.; Li, L.; Song, H.; Wang, J.; Wu, Q. A Droplet-Based Microfluidic Electrochemical Sensor Using Platinum-Black Microelectrode and its Application in High Sensitive Glucose Sensing. *Biosens. Bioelectron.* **2014**, *55*, 106−112.

(4) Rusling, J. F. Developing Microfluidic Sensing Devices Using 3D Printing. *ACS Sens.* **2018**, *3*, 522−526.

(5) Gómez-Sjöberg, R.; Leyrat, A. A.; Pirone, D. M.; Chen, C. S.; Quake, S. R. Versatile, Fully Automated, Microfluidic Cell Culture System. *Anal. Chem.* **2007**, *79*, 8557−8563.

(6) Munshi, A. S.; Chen, C.; Townsend, A. D.; Martin, R. S. Use of 3D Printing and Modular Microfluidics to Integrate Cell Culture, Injections and Electrochemical Analysis. *Anal. Methods* **2018**, *10*, 3364−3374.

(7) Chen, C.; Townsend, A. D.; Hayter, E. A.; Birk, H. M.; Sell, S. A.; Martin, R. S. Insert-Based Microfluidics for 3D Cell Culture with Analysis. *Anal. Bioanal. Chem.* **2018**, *410*, 3025−3035.

(8) Männel, M. J.; Fischer, C.; Thiele, J. A Non-Cytotoxic Resin for Micro-Stereolithography for Cell Cultures of HUVECs. *Micromachines* **2020**, *11*, No. 246.

(9) Ulkir, O.; Girit, O.; Ertugrul, I. Design and Analysis of a Laminar Diffusion-Based Micromixer with Microfluidic Chip. *J. Nanomater.* **2021**, *2021*, No. 6684068.

(10) Catarino, S. O.; Rodrigues, R. O.; Pinho, D.; Miranda, J. M.; Minas, G.; Lima, R. Blood Cells Separation and Sorting Techniques of Passive Microfluidic Devices: From Fabrication to Applications. *Micromachines* **2019**, *10*, No. 593.

(11) Mitxelena-Iribarren, O.; Zabalo, J.; Arana, S.; Mujika, M. Improved Microfluidic Platform for Simultaneous Multiple Drug Screening Towards Personalized Treatment. *Biosens. Bioelectron.* **2019**, *123*, 237−243.

(12) Eduati, F.; Utharala, R.; Madhavan, D.; Neumann, U. P.; Longerich, T.; Cramer, T.; Saez-Rodriguez, J.; Merten, C. A. A Microfluidics Platform for Combinatorial Drug Screening on Cancer Biopsies. *Nat. Commun.* **2018**, *9*, No. 2434.

(13) Pandya, H. J.; Dhingra, K.; Prabhakar, D.; Chandrasekar, V.; Natarajan, S. K.; Vasan, A. S.; Kulkarni, A.; Shafiee, H. A Microfluidic Platform for Drug Screening in a 3D Cancer Microenvironment. *Biosens. Bioelectron.* **2017**, *94*, 632−642.

(14) Santana, H. S.; Palma, M. S. A.; Lopes, M. G. M.; Souza, J.; Lima, G. A. S.; Taranto, O. P.; Silva, J. L. Microfluidic Devices and 3D Printing for Synthesis and Screening of Drugs and Tissue Engineering. *Ind. Eng. Chem. Res.* **2020**, *59*, 3794−3810.

(15) Ai, Y.; Xie, R.; Xiong, J.; Liang, Q. Microfluidics for Biosynthesizing: From Droplets and Vesicles to Artificial Cells. *Small* **2020**, *16*, No. 1903940.

(16) Bhattacharjee, N.; Urrios, A.; Kang, S.; Folch, A. The Upcoming 3D-Printing Revolution in Microfluidics. *Lab Chip* **2016**, *16*, 1720−1742.

(17) Yazdi, A. A.; Popma, A.; Wong, W.; Nguyen, T.; Pan, Y.; Xu, J. 3D Printing: An Emerging Tool for Novel Microfluidics and Lab-on-a-Chip Applications. *Microfluid. Nanofluid.* **2016**, *20*, 50.

(18) Ho, C. M. B.; Ng, S. H.; Li, K. H. H.; Yoon, Y.-J. 3D Printed Microfluidics for Biological Applications. *Lab Chip* **2015**, *15*, 3627−3637.

(19) Pan, Y.; Zhou, C.; Chen, Y. A Fast Mask Projection Stereolithography Process for Fabricating Digital Models in Minutes. *J. Manuf. Sci. Eng.* **2012**, *134*, No. 051011.

(20) De Beer, M. P.; Van Der Laan, H. L.; Cole, M. A.; Whelan, R. J.; Burns, M. A.; Scott, T. F. Rapid, Continuous Additive Manufacturing by Volumetric Polymerization Inhibition Patterning. *Sci. Adv.* **2019**, *5*, No. eaau8723.

(21) Männel, M. J.; Hauck, N.; Thiele, J. Solvent-Resistant Microfluidic Devices Made from PFHDA Resins by Micro-Stereolithography. *Proc. SPIE* **2020**, *11235*, No. 112350H.

(22) Wallin, T. J.; Pikul, J. H.; Bodkhe, S.; Peele, B. N.; Mac Murray, B. C.; Therriault, D.; McEnerney, B. W.; Dillon, R. P.; Giannelis, E. P.; Shepherd, R. F. Click Chemistry Stereolithography for Soft Robots that Self-Heal. *J. Mater. Chem. B* **2017**, *5*, 6249−6255.

(23) Yang, C.; Boorugu, M.; Dopp, A.; Ren, J.; Martin, R.; Han, D.; Choi, W.; Lee, H. 4D Printing Reconfigurable, Deployable and Mechanically Tunable Metamaterials. *Mater. Horiz.* **2019**, *6*, 1244−1250.

(24) Zhang, B.; Zhang, W.; Zhang, Z.; Zhang, Y.-F.; Hingorani, H.; Liu, Z.; Liu, J.; Ge, Q. Self-Healing Four-Dimensional Printing with an Ultraviolet Curable Double-Network Shape Memory Polymer System. *ACS Appl. Mater. Interfaces* **2019**, *11*, 10328−10336.

(25) Han, D.; Farino, C.; Yang, C.; Scott, T.; Browe, D.; Choi, W.; Freeman, J. W.; Lee, H. Soft Robotic Manipulation and Locomotion with a 3D Printed Electroactive Hydrogel. *ACS Appl. Mater. Interfaces* **2018**, *10*, 17512−17518.

(26) Han, D.; Lu, Z.; Chester, S. A.; Lee, H. Micro 3D Printing of a Temperature-Responsive Hydrogel Using Projection Micro-Stereolithography. *Sci. Rep.* **2018**, *8*, No. 1963.

(27) Xu, T.; Zhang, J.; Salehizadeh, M.; Onaizah, O.; Diller, E. Millimeter-Scale Flexible Robots with Programmable Three-Dimensional Magnetization and Motions. *Sci. Robot.* **2019**, *4*, No. eaav4494.

(28) Han, D.; Yang, C.; Fang, N. X.; Lee, H. Rapid Multi-Material 3D Printing with Projection Micro-Stereolithography using Dynamic Fluidic Control. *Addit. Manuf.* **2019**, *27*, 606−615.

(29) Kowsari, K.; Akbari, S.; Wang, D.; Fang, N. X.; Ge, Q. High-Efficiency High-Resolution Multimaterial Fabrication for Digital Light Processing-Based Three-Dimensional Printing. *3D Print. Addit. Manuf.* **2018**, *5*, 185−193.

(30) Zhou, C.; Chen, Y.; Yang, Z.; Khoshnevis, B. Development of a Multi-Material Mask-Image-Projection-Based Stereolithography for the Fabrication of Digital Materials. *Proceedings of Annual Solid Freeform Fabrication Symposium*, Austin, TX, 2011.
(31) Sun, C.; Fang, N.; Wu, D.; Zhang, X. Projection Micro-Stereolithography Using Digital Micro-Mirror Dynamic Mask. *Sens. Actuators, A* **2005**, *121*, 113−120.
(32) Razavi Bazaz, S.; Rouhi, O.; Raoufi, M. A.; Ejeian, F.; Asadnia, M.; Jin, D.; Ebrahimi Warkiani, M. 3D Printing of Inertial Microfluidic Devices. *Sci. Rep.* **2020**, *10*, No. 5929.
(33) Männel, M. J.; Selzer, L.; Bernhardt, R.; Thiele, J. Optimizing Process Parameters in Commercial Micro-Stereolithography for Forming Emulsions and Polymer Microparticles in Nonplanar Microfluidic Devices. *Adv. Mater. Technol.* **2019**, *4*, No. 1800408.
(34) Gong, H.; Beauchamp, M.; Perry, S.; Woolley, A. T.; Nordin, G. P. Optical Approach to Resin Formulation for 3D printed Microfluidics. *RSC Adv.* **2015**, *5*, 106621−106632.
(35) Gong, H.; Bickham, B. P.; Woolley, A. T.; Nordin, G. P. Custom 3D Printer and Resin for 18 μm × 20 μm Microfluidic Flow Channels. *Lab Chip* **2017**, *17*, 2899−2909.
(36) Luongo, A.; Falster, V.; Doest, M. B.; Ribo, M. M.; Eiriksson, E. R.; Pedersen, D. B.; Frisvad, J. R. Microstructure Control in 3D Printing with Digital Light Processing. *Comput. Graphics Forum* **2020**, *39*, 347−359.
(37) Kowsari, K.; Zhang, B.; Panjwani, S.; Chen, Z.; Hingorani, H.; Akbari, S.; Fang, N. X.; Ge, Q. Photopolymer Formulation to Minimize Feature Size, Surface Roughness, and Stair-Stepping in Digital Light Processing-Based Three-Dimensional Printing. *Addit. Manuf.* **2018**, *24*, 627−638.
(38) Au, A. K.; Bhattacharjee, N.; Horowitz, L. F.; Chang, T. C.; Folch, A. 3D-Printed Microfluidic Automation. *Lab Chip* **2015**, *15*, 1934−1941.
(39) Gong, H.; Woolley, A. T.; Nordin, G. P. High Density 3D Printed Microfluidic Valves, Pumps, and Multiplexers. *Lab Chip* **2016**, *16*, 2450−2458.
(40) Rogers, C. I.; Oxborrow, J. B.; Anderson, R. R.; Tsai, L.-F.; Nordin, G. P.; Woolley, A. T. Microfluidic Valves Made from Polymerized Polyethylene Glycol Diacrylate. *Sens. Actuators, B* **2014**, *191*, 438−444.
(41) Rogers, C. I.; Qaderi, K.; Woolley, A. T.; Nordin, G. P. 3D Printed Microfluidic Devices with Integrated Valves. *Biomicrofluidics* **2015**, *9*, No. 016501.
(42) Lee, Y.-S.; Bhattacharjee, N.; Folch, A. 3D-Printed Quake-Style Microvalves and Micropumps. *Lab Chip* **2018**, *18*, 1207−1214.
(43) Männel, M. J.; Weigel, N.; Thiele, J. Multifunctional Microfluidic Devices from Tailored Photopolymer Formulations. *Proc. SPIE* **2019**, *10875*, No. 1087507.
(44) Bhattacharjee, N.; Parra-Cabrera, C.; Kim, Y. T.; Kuo, A. P.; Folch, A. Desktop-Stereolithography 3D-Printing of a Poly(dimethylsiloxane)-Based Material with Sylgard-184 Properties. *Adv. Mater.* **2018**, *30*, No. 1800001.
(45) Gonzalez, G.; Chiappone, A.; Dietliker, K.; Pirri, C. F.; Roppolo, I. Fabrication and Functionalization of 3D Printed Polydimethylsiloxane-Based Microfluidic Devices Obtained through Digital Light Processing. *Adv. Mater. Technol.* **2020**, *5*, No. 2000374.
(46) Patel, D. K.; Sakhaei, A. H.; Layani, M.; Zhang, B.; Ge, Q.; Magdassi, S. Highly Stretchable and UV Curable Elastomers for Digital Light Processing Based 3D Printing. *Adv. Mater.* **2017**, *29*, No. 1606000.
(47) Zhang, Y.-F.; Ng, C. J.-X.; Chen, Z.; Zhang, W.; Panjwani, S.; Kowsari, K.; Yang, H. Y.; Ge, Q. Miniature Pneumatic Actuators for Soft Robots by High-Resolution Multimaterial 3D Printing. *Adv. Mater. Technol.* **2019**, *4*, No. 1900427.
(48) Vaicekauskaite, J.; Mazurek, P.; Vudayagiri, S.; Skov, A. L. Mapping the Mechanical and Electrical Properties of Commercial Silicone Elastomer Formulations for Stretchable Transducers. *J. Mater. Chem. C* **2020**, *8*, 1273−1279.
(49) Abate, A. R.; Romanowsky, M. B.; Agresti, J. J.; Weitz, D. A. Valve-Based Flow Focusing for Drop Formation. *Appl. Phys. Lett.* **2009**, *94*, No. 023503.
(50) Peng, B.; Yang, Y.; Gu, K.; Amis, E. J.; Cavicchi, K. A. Digital Light Processing 3D Printing of Triple Shape Memory Polymer for Sequential Shape Shifting. *ACS Mater. Lett.* **2019**, *1*, 410−417.
(51) Tiller, B.; Reid, A.; Zhu, B.; Guerreiro, J.; Domingo-Roca, R.; Curt Jackson, J.; Windmill, J. F. C. Piezoelectric Microphone via a Digital Light Processing 3D Printing Process. *Mater. Des.* **2019**, *165*, No. 107593.
(52) Zhang, B.; Li, S.; Hingorani, H.; Serjouei, A.; Larush, L.; Pawar, A. A.; Goh, W. H.; Sakhaei, A. H.; Hashimoto, M.; Kowsari, K.; Magdassi, S.; Ge, Q. Highly Stretchable Hydrogels for UV Curing Based High-Resolution Multimaterial 3D Printing. *J. Mater. Chem. B* **2018**, *6*, 3246−3253.
(53) Ding, R.; Du, Y.; Goncalves, R. B.; Francis, L. F.; Reineke, T. M. Sustainable near UV-Curable Acrylates Based on Natural Phenolics for Stereolithography 3D printing. *Polym. Chem.* **2019**, *10*, 1067−1077.
(54) Kotz, F.; Risch, P.; Helmer, D.; Rapp, B. E. Highly Fluorinated Methacrylates for Optical 3D Printing of Microfluidic Devices. *Micromachines* **2018**, *9*, No. 115.
(55) Socrates, G. *Infrared and Raman Characteristic Group Frequencies: Tables and Charts*, 3rd ed.; John Wiley & Sons, Inc.: Chichester, 2004.
(56) Benmessaoud, N.; Hamri, S.; Bouchaour, T.; Maschke, U. Swelling and Thermal Behavior of a Cross-Linked Polymer Networks Poly(2-Phenoxyethyl Acrylate): Exploitation by the Voigt Viscoelastic Model. *Polym. Bull.* **2020**, *77*, 5567−5588.
(57) Roach, D. J.; Kuang, X.; Yuan, C.; Chen, K.; Qi, H. J. Novel Ink for Ambient Condition Printing of Liquid Crystal Elastomers for 4D Printing. *Smart Mater. Struct.* **2018**, *27*, No. 125011.
(58) Hingorani, H.; Zhang, Y.-F.; Zhang, B.; Serjouei, A.; Ge, Q. Modified Commercial UV Curable Elastomers for Passive 4D printing. *Int. J. Smart Nano Mater.* **2019**, *10*, 225−236.
(59) Roach, D. J.; Hamel, C. M.; Dunn, C. K.; Johnson, M. V.; Kuang, X.; Qi, H. J. The m4 3D Printer: A Multi-Material Multi-Method Additive Manufacturing Platform for Future 3D Printed Structures. *Addit. Manuf.* **2019**, *29*, No. 100819.
(60) Young, A. J.; Guillet-Nicolas, R.; Marshall, E. S.; Kleitz, F.; Goodhand, A. J.; Glanville, L. B. L.; Reithofer, M. R.; Chin, J. M. Direct Ink Writing of Catalytically Active UiO-66 Polymer Composites. *Chem. Commun.* **2019**, *55*, 2190−2193.
(61) Lazauskas, A.; Jucius, D.; Baltrušaitis, V.; Gudaitis, R.; Prosyčevas, I.; Abakevičienė, B.; Guobienė, A.; Andrulevičius, M.; Grigaliūnas, V. Shape-Memory Assisted Scratch-Healing of Transparent Thiol-Ene Coatings. *Materials (Basel)* **2019**, *12*, No. 482.
(62) Frewin, C. L.; Ecker, M.; Joshi-Imre, A.; Kamgue, J.; Waddell, J.; Danda, V. R.; Stiller, A. M.; Voit, W. E.; Pancrazio, J. J. Electrical Properties of Thiol-ene-based Shape Memory Polymers Intended for Flexible Electronics. *Polymers* **2019**, *11*, No. 902.
(63) Chen, L.; Wu, Q.; Wei, G.; Liu, R.; Li, Z. Highly Stable Thiol−ene Systems: From Their Structure−Property Relationship to DLP 3D Printing. *J. Mater. Chem. C* **2018**, *6*, 11561−11568.
(64) Li, Z.; Wang, C.; Qiu, W.; Liu, R. Antimicrobial Thiol−ene−Acrylate Photosensitive Resins for DLP 3D Printing. *Photochem. Photobiol.* **2019**, *95*, 1219−1229.
(65) Wang, C.; Wang, C.; Li, Z. Thiol-ene-acrylate Ternary Photosensitive Resins for DLP 3D Printing. *J. Photopolym. Sci. Technol.* **2020**, *33*, 285−290.
(66) He, Y.; Zhang, F.; Saleh, E.; Vaithilingam, J.; Aboulkhair, N.; Begines, B.; Tuck, C. J.; Hague, R. J. M.; Ashcroft, I. A.; Wildman, R. D. A Tripropylene Glycol Diacrylate-Based Polymeric Support Ink for Material Jetting. *Addit. Manuf.* **2017**, *16*, 153−161.
(67) Touchet, T. J.; Cosgriff-Hernandez, E. M. Hierarchal Structure−Property Relationships of Segmented Polyurethanes. In *Advances in Polyurethane Biomaterials*; Cooper, S. L., Guan, J., Eds.; Woodhead Publishing, 2016; pp 3−22.

https://doi.org/10.1021/acsami.1c05547
ACS Appl. Mater. Interfaces 2021, 13, 31086−31101

(68) Baret, J.-C. Surfactants in Droplet-Based Microfluidics. *Lab Chip* **2012**, *12*, 422−433.
(69) Wagner, O.; Thiele, J.; Weinhart, M.; Mazutis, L.; Weitz, D. A.; Huck, W. T. S.; Haag, R. Biocompatible Fluorinated Polyglycerols for Droplet Microfluidics as an Alternative to PEG-based Copolymer Surfactants. *Lab Chip* **2016**, *16*, 65−69.
(70) Hauck, N.; Seixas, N.; Centeno, S. P.; Schlüßler, R.; Cojoc, G.; Müller, P.; Guck, J.; Wöll, D.; Wessjohann, L. A.; Thiele, J. Droplet-Assisted Microfluidic Fabrication and Characterization of Multifunctional Polysaccharide Microgels Formed by Multicomponent Reactions. *Polymers* **2018**, *10*, No. 1055.

https://doi.org/10.1021/acsami.1c05547
ACS Appl. Mater. Interfaces 2021, 13, 31086−31101